

Aerospace Vehicle Design

Final report

Academics responsible: Dr. Errikos Levis and Dr. Robert Hewson
Department: Department of Aeronautics
Course: A401 MEng in Aeronautics
Module: AE3 Aerospace Vehicle Design
Academic year: 2018/2019
Students: Maïlys Buquet - 01198845
Pietro Giraudi - 01202919
Ioannis Karatsivoulis - 01220580
Łukasz Śliwiński - 01240212
Group: 14
Date: 07/12/2018

Department of Aeronautics
South Kensington Campus
Imperial College London
London SW7 2AZ
U.K.

Contents

Contents	1
List of Figures	4
List of Tables	5
1 Introduction	7
2 Wing Design	7
2.1 Area S_{ref}	7
2.2 Wingspan b	7
2.3 Aspect Ratio \mathcal{R}	7
2.4 Airfoil selection	7
2.4.1 Design lift coefficient	8
2.4.2 Thickness to chord ratio	8
2.4.3 Supercritical capabilities	8
2.4.4 Final considerations on the airfoil selection	8
2.5 Sweep Λ	9
2.6 Taper ratio λ and twist	10
2.7 Wing Incidence i_W	10
2.8 Dihedral Γ	10
2.9 Wing Vertical Location	10
2.10 Final design parameters and optimisation	11
3 Aerodynamic Analysis - Wing Lift	11
3.1 Clean airfoil aerodynamic analysis	11
3.1.1 Airfoil lift curve in takeoff/landing	11
3.1.2 Airfoil lift curve in cruise	12
3.2 Preliminary high lift devices selection and parameter choice	12
3.3 Airfoil aerodynamic lift analysis with high lift devices	12
3.3.1 Airfoil lift increment due to high lift devices ΔC_l	13
3.3.2 Airfoil lift curve slope due to flaps $(C_{l\alpha})_\delta$	13
3.3.3 Airfoil maximum lift increment due to flaps (ΔC_{lmax})	13
3.3.4 Construction of airfoil lift curve: flaps down	14
3.4 Clean wing aerodynamic analysis	15
3.5 Wing aerodynamic lift analysis with high lift devices	16
3.5.1 Wing lift increment due to high lift devices ΔC_{lmax}	16
3.5.2 Wing lift curve slope due to flaps $(C_{L\alpha W})_\delta$	16
3.5.3 Wing maximum lift increment due to flaps ΔC_{LmaxW}	16
3.5.4 Construction of wing lift curve: flaps down	17
3.5.5 Construction of wing lift curve: flaps down	18
4 Tailplane sizing and design	18
4.1 Overview	18
4.2 Horizontal tailplane	18
4.2.1 Area	19
4.2.2 Airfoil selection	19
4.2.3 Sweep $\Lambda_{\frac{\varepsilon}{4}}$	20
4.2.4 Aspect ratio	20
4.2.5 Taper ratio λ	20
4.2.6 Dihedral angle	20

4.2.7	Twist	20
4.3	Vertical tailplane	20
4.3.1	Area	20
4.3.2	Airfoil selection	21
4.3.3	Aspect ratio \mathcal{R}_v	21
4.3.4	Taper ratio λ_v	21
4.3.5	Sweep Λ_4^ε	21
5	Power plant selection (do not mark)	21
5.1	Selection	21
5.2	Integration	22
5.2.1	Inlet	22
5.2.2	Nozzle	22
5.2.3	Thrust reverser	22
5.3	Dimensions	22
5.4	Auxiliary Power Unit	22
6	Control surface design	22
6.1	Ailerons	23
6.2	Elevator	23
6.3	Rudder	23
6.4	Summary of control surface parameters	24
7	Static stability and trim analysis	24
7.0.1	Longitudinal static stability	24
7.0.2	Directional-Lateral static stability	25
7.1	Trim	25
8	Fuselage design & sizing	26
8.1	Fuselage cabin	26
8.2	Fuselage section optimization	28
8.3	Helicopter considerations	28
8.4	Pallet considerations	29
8.5	Troops considerations	29
8.6	Fuselage doors	29
8.7	Fuselage nose cone	29
8.8	Fuselage tail	30
9	Aircraft system layout design	30
9.1	Flight Control system	30
9.2	Fuel system	31
9.3	Hydraulic system	34
9.4	Electrical system	34
9.5	Environmental control system	34
9.5.1	Pressurization system	34
9.5.2	Pneumatic system	34
9.5.3	Air-conditioning system	34
9.5.4	Oxygen system	34
9.6	Avionics system	34
9.7	Other systems	34
9.7.1	Anti-icing system	34
9.7.2	Rain removal and defog system	35

10 Weight & balance predictions	35
10.1 CG envelope	35
11 Aerodynamic analysis - Drag Estimation	37
11.1 Parasite (Zero-Lift) Drag Prediction	37
11.1.1 Main Components	37
11.1.2 Miscellaneous Drags	38
11.1.3 Leakage and Protuberance Drag	39
11.2 Induced (Lift Dependant) Drag	39
11.3 Wave drag	39
11.4 Total Drag Coefficient	40
12 Performance Estimation	40
12.1 Take-off distance	40
12.1.1 Ground Roll S_G	41
12.1.2 Rotation distance S_R	41
12.1.3 Transition distance S_{TR}	41
12.1.4 Climb to obstacle height S_{CL}	41
12.1.5 Total take-off distances	41
12.2 Balanced Field Length	42
12.3 Landing Distance	42
12.3.1 Approach	42
12.3.2 Flare	42
12.3.3 Rolling	42
12.3.4 Braking	42
12.3.5 Total landing distances	43
12.4 Mission performance	43
12.5 Point performance	43
12.6 Flight envelope	43
References	45

List of Figures

1	Sketch of half wing depicting the essential planform parameters: b represents the wingspan, λ represents the taper ratio and $\Lambda_{c/4}$ represents the sweep angle of the quarter chord line.	7
2	Effect of sweep on the critical Mach number of the wing	9
3	Effect of sweep on aerodynamic efficiency. [1] [2]	9
4	Wing sweep historical trend. [3]	9
5	Lift distribution at 0° angle of attack computed with a vortex lattice method. This is the result of several iterations where small changes in the twist distribution and in the taper ratio were used to approximate an elliptical distribution.	10
6	Lift curve of the airfoil computed with XFOIL for $Re = 2.195 \times 10^7$ and $M = 0.17$	11
7	Lift curve of the airfoil computed with XFOIL for $Re = 1.679 \times 10^7$ and $M = 0.79$	12
8	Predicted lift curve of the airfoil with high lift devices in landing configuration.	14
9	Predicted lift curve of the airfoil with high lift devices in takeoff configuration.	15
10	Computed clean wing lift curve at Mach 0.79.	15
11	Computed clean wing lift curve at Mach 0.17.	16
12	Predicted lift curve of the wing with high lift devices in landing configuration.	17
13	Predicted lift curve of the wing with high lift devices in takeoff configuration.	18
14	Horizontal tail positioning [3]	19
15	Empirical aileron sizing curve [3]	23
16	i_H , with the helicopter, for cruise	25
17	i_H , with the pallets, for cruise	25
18	i_H , with the troops, for cruise	26
19	i_H , with the helicopter, for landing	26
20	i_H , with the troops, for landing	26
21	i_H , with the pallets, for landing	26
22	Top and side view of the fuselage	26
23	Fuselage cross-section	27
24	Conic curves geometry (lateral symmetry)	27
25	Cabin layout for helicopter	27
26	Cabin layout for pallets	27
27	Cabin layout for troops	27
28	Trapezoid dictating fuselage cross-section	27
29	Relation between conic curve parameter and ratios	28
30	Relation between conic curve parameter and drag penalty	28
31	Fuselage exit door layout	29
32	Side view of the fuselage nose	30
33	Cockpit windshield dimensions	30
34	Actuators layout	31
35	Fuel tanks layout	32
36	Fuel system schematic	32
37	Hydraulic system schematic	33
38	electrical system schematic	33
39	Variation of x-CG position during mission for three loading cases	36
40	Cruise range performance	43
41	Excess Power P_S plot, in ft.min^{-1}	44

List of Tables

1	Summary of the wing parameters.	11
2	Airfoil lift parameters for $Re = 2.195 \times 10^7$ and $M = 0.17$	11
3	Airfoil lift parameters for $Re = 1.679 \times 10^7$ and $M = 0.79$	12
4	High lift devices parameters in landing configuration. These parameters were found after various iterations and are the ones that satisfy our minimum requirements.	12
5	High lift devices parameters in takeoff configuration. These parameters were found after various iterations and are the ones that satisfy our minimum requirements.	12
6	Airfoil lift increment due to Fowler flaps in landing configuration.	13
7	Airfoil lift increment due to Fowler flaps in takeoff configuration.	13
8	Airfoil lift increment due to leading edge slats in landing configuration.	13
9	Airfoil lift curve slope due to high lift devices in landing and takeoff configuration.	13
10	Airfoil maximum lift increment due to Fowler flaps in landing configuration.	14
11	Airfoil maximum lift increment due to Fowler flaps in takeoff configuration.	14
12	Airfoil maximum lift increment due to leading edge slats in landing and takeoff configurations.	14
13	Wing lift increment due to high lift devices in landing configuration.	16
14	Wing lift increment due to high lift devices in takeoff configuration.	16
15	Wing lift curve slope due to flaps.	16
16	Wing maximum lift increment due to Fowler flaps in landing configuration.	17
17	Wing maximum lift increment due to Fowler flaps in takeoff configuration.	17
18	Wing maximum lift increment due to leading edge slats.	17
19	The horizontal tailplane's 3D lift curve slope.	20
20	Summary of the main tailplane parameters	21
21	Engine parameters, scale factor 0.78	22
22	Summary of chosen engine area values	22
23	Auxiliary Power Unit dimensions and mass	22
24	Summary of control surface design characteristics	24
25	Static stability analysis for different loading configurations	25
26	Exit dimensions used. The type in the brackets corresponds to the FAR 25 exit type that dictates the minimum exit dimensions (see Reference [4]).	29
27	Weight estimation "fudge factors" due to the application of advanced materials [3].	35
28	Component weight and x-CG positions	36
29	Reasoning behind estimating CG positions of aircraft components	37
30	Values of coefficients used in Equation (11) for parasitic drag of main components.	37
31	Values of friction and drag coefficients for subsonic cruise at Mach number $M = 0.79$. S_{ref} used to obtain C_{D0c} is $2260.4ft^2$. To account for possible roughness of surfaces, C_{fc} were computed using the lowest of actual and cut-off Reynolds numbers for each components, as explained in Reference [3].	38
32	Values of friction and drag coefficients for subsonic take-off and landing. S_{ref} used to obtain C_{D0c} is $2260.4ft^2$. Values for take-off and landing are rather close as the Mach numbers at Mach number $M = 0.17$ at these points of the mission are very close.	38
33	Values of miscellaneous drag coefficients for different components in the subsonic regime.	38
34	Total miscellaneous drag coefficients for three phases of the flight: cruise, take-off and landing. Note that take-off and even more particularly landing have high values due to the high deflection of the flaps.	39
35	Values of induced drag coefficients from Oswald efficiency based and suction methods. Values for cruise are different as the drag-due-to-lift factors K are obtained by different ways. Also, take-off and landing values are higher for the suction method, which also includes ground effects, generating more lift.	39
36	Values of drag coefficients, using both Oswald efficiency based and suction method for C_{Di} . Values of $C_{D_{total}}$ for take-off and landing are notably high, which could be explained by the flaps deflection impacting C_{D0} and the lift generated impacting C_{Di}	40

37	Values of take-off distances and their components for both runways. Distances are in meters. A safety factor of 1.5 was applied. Both S_{TO} are smaller than their respective runways, of 1.5km and 1km. Therefore, both take-off can be achieved.	41
38	Values of landing distances and their component for both runways. Distances are in meters. Both S_L are smaller than their respective runways, of 1.5km and 1km. Therefore, both landings can be achieved.	43

1 Introduction

The objective of this project was to do the conceptual design for a conventional military jet transport. Building on the results of the initial sizing presented in the early stages of the design, this final report outlines the iterative process employed with its background reasoning, and the results obtained. This conceptual design includes wing design, aerodynamic analysis of the wing, tailplane sizing and design, power plant selection, control surface design, static stability and trim analysis, fuselage design and sizing, aircraft system layout design, weight and balance predictions, and finally drag and performance estimation. During this design process we either confirmed or discarded the assumptions made during the early stages of the design and the ones considered wrong or inaccurate, were changed in order to better match the design requirements imposed by airworthiness regulations and design specifications.

2 Wing Design

In this section, the procedure used to design the wing will be outlined and the results will be discussed. The entire wing design process started from the values for the wing loading and the maximum takeoff weight defined in the conceptual design.

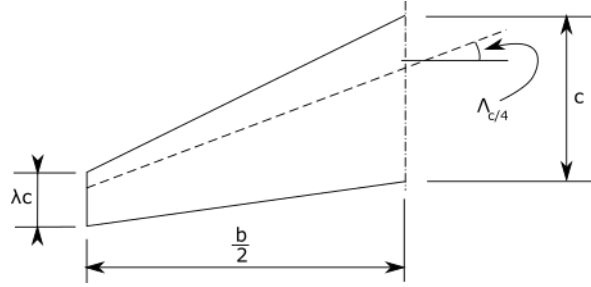


Figure 1: Sketch of half wing depicting the essential planform parameters: b represents the wingspan, λ represents the taper ratio and $\Lambda_{c/4}$ represents the sweep angle of the quarter chord line.

2.1 Area S_{ref}

Our wing design started by defining the wing area necessary to meet the flight constraints. Given the design wing loading ($\frac{W}{S}$) of 3495 N/m² and the *MTOW* of 74800 kg, the resultant wing area required, calculated with equation 1, is 209.95 m². This value was then taken as the reference area (S_{ref}) for further calculations.

$$S_{ref} = \frac{MTOW g}{\left(\frac{W}{S}\right)} \quad (1)$$

2.2 Wingspan b

For practical reasons, we do not want our wingspan to be wider than 40 meters. This value is a limit we defined as we are requested to service an unprepared runway where the width of the runway is not known. The main reason for this choice is obstacle clearance during takeoff, landing and taxi from the unprepared runway.

2.3 Aspect Ratio \mathcal{R}

The aspect ratio of a wing is a parameter directly affecting the aerodynamic efficiency of an aircraft. With a simple derivation it can be shown that by maximising the aspect ratio of a wing we minimise the induced drag, therefore, we decided to maximise the aspect ratio of our wing without exceeding the limit on the wingspan previously defined. Clearly, in our case, the maximum aspect ratio is obtained when the wingspan is set at exactly 40 m. The resultant aspect ratio is then 7.62.

2.4 Airfoil selection

The airfoil is one of the core decisions that the wing designer has to take when approaching the wing design problem. This choice, generally, is affected by many different parameters and the duty of the designer is to find an airfoil that satisfies the majority of the requirements. In many case, some of the parameters on which the choice of the airfoil is based are conflicting or complementary (a good example is: high second moment or

area for structural integrity vs low drag requirement), this is the reason why, in many cases the designer must generate a new airfoil shape to suits his needs. The drawback of this is that it is a long process mainly based on aerodynamic research and testing. In our case we do not have the resources or time to design an airfoil shape for our needs, therefore, our airfoil will be selected between the ones of public domain for which good resources are available.

2.4.1 Design lift coefficient

The first driving parameter in choosing an airfoil is the design lift coefficient. This is the coefficient at which the airfoil is going to work during the majority of the flight. A well-designed airfoil must also minimise the drag at its design C_l as the lift to drag ratio (L/D) is a direct indicator of the aerodynamic efficiency of the wing (the higher the lift to drag ratio the higher the efficiency).

As a first approximation of this parameter, we assumed the wing lift coefficient C_L to be equal to the airfoil lift coefficient C_l . This assumption will be relaxed later to refine and optimize the design point.

The design lift coefficient is therefore:

$$C_l = \frac{2}{\rho U^2} \left(\frac{W}{S} \right) \quad (2)$$

As we can see from equation 2, the lift coefficient is a function of the air density which is a function of altitude. The problem with this is that, in general, airfoils have a well defined C_l at which the efficiency is maximised and this parameter is constant during the flight. To overcome this problem we decided to cruise-climb in order to have our wing constantly working at its maximum potential.

Given the parameters of our cruise (starting altitude: 37000 ft, Mach number: 0.79) and the design parameters previously defined ($\frac{W}{S}$), it is possible to confirm that our design lift coefficient is 0.3528.

2.4.2 Thickness to chord ratio

The thickness to chord ratio is a parameter directly affecting the structural integrity of the wing. In principle the higher the thickness to chord ratio, the higher the second moment of area and therefore the less material is required to withstand the load. On the other hand, the thickness to chord ratio is highly affecting the drag of the wing, especially in the transonic regime. To find a good balance between these parameters, we therefore wrote an optimisation script. In such script the wing was idealised as a cantilever beam and given the loads it was possible to find the best thickness to chord ratio for different materials (we used CFRP and aluminium) from both a structural and aerodynamic perspective. Using this script we found that a thickness to chord ratio of 10%-12% was a good compromise.

2.4.3 Supercritical capabilities

The last point to consider in our selection is the working Mach number. The speed required by the customer is of 0.79 Mach during cruise and 0.82 Mach for maximum speed. These two regimes are above the critical Mach number of many subsonic airfoils so the designer decided to apply sweep to the wing and also opted for a supercritical airfoil.

2.4.4 Final considerations on the airfoil selection

From the previous considerations, two airfoils were found to satisfy our needs:

- NASA SC(2)-0410;
- NASA SC(2)-0412.

These two airfoils were developed in the late 60s/early 70s by the NASA institute to meet the new supercritical requirements of that time. They both have a critical Mach number higher than 0.78, which means that with some degrees of sweep we can safely meet the speed requirements and they are both optimised for a lift coefficient of 0.4 [5]. At this point, we checked how much volume was required by our systems and fuel tanks and we found that this requirement was safely met by the airfoil NASA SC(2)-0410, so we decided that this one was our final airfoil shape.

2.5 Sweep Λ

The main idea of a swept wing is to delay the drag divergence to a Mach number higher than the critical Mach number of the airfoil [6]. If we consider a swept wing like the one sketched in Figures 2 we can observe that the normal flow velocity relative to the airfoil section of the wing is $M_\infty \cos \Lambda$. As a consequence of this the free stream critical Mach number can be increased above the M_{crit} of the airfoil. Following this reasoning, the critical Mach number of the overall swept wing is increased to $M_{crit}/\cos \Lambda$. This simple reasoning is clearly an oversimplification of the real-life flow over a swept wing but it can be used as a limit in the first stages of the wing design. In real life the actual critical number of a 3D swept wing is:

$$M_{crit,air\,foil} < M_{crit,swept} < \frac{M_{crit,air\,foil}}{\cos \Lambda} \quad (3)$$

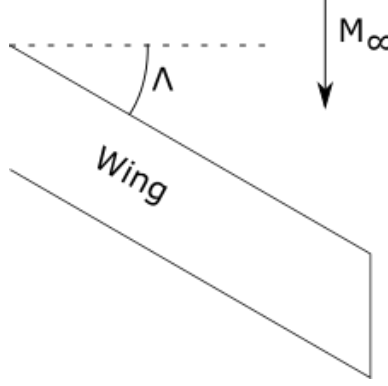


Figure 2: Effect of sweep on the critical Mach number of the wing

Even if sweeping the wing is important to reduce the drag in transonic flight, it entails also some aerodynamic disadvantages, as increasing the sweep also reduces the lift generated by the wing [6], and structural disadvantages. As we can observe on the Figures 4 there is also a clear variation in L/D with increasing the sweep angle. The duty of the designer is therefore to find the correct balance between advantages and disadvantages to find the optimum design solution.

The M_{crit} of the airfoil used in our wing (NASA SC(2)-0410) is 0.78, so to reach the maximum velocity requirement of Mach 0.82 we decided to sweep our wing. Ideally, we wanted to design a wing with a critical Mach number just above 0.82 but it is very difficult to predict with precision the critical Mach number of the final design so we decided the sweep angle keeping a safety margin of few degrees. Given these premises and considering historical trends (figure 4) we opted for a sweep angle at the quarter-chord line of 25° .

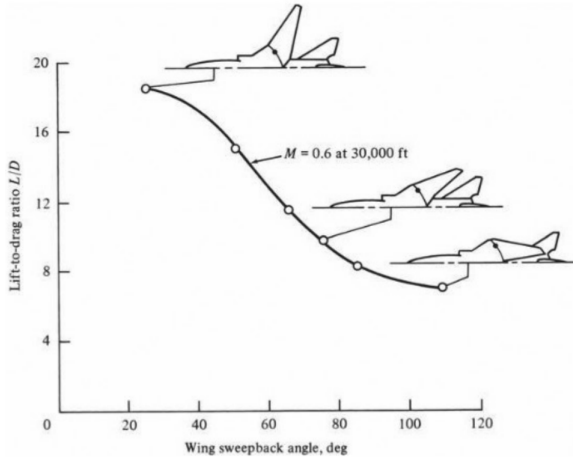


Figure 3: Effect of sweep on aerodynamic efficiency. [1] [2]

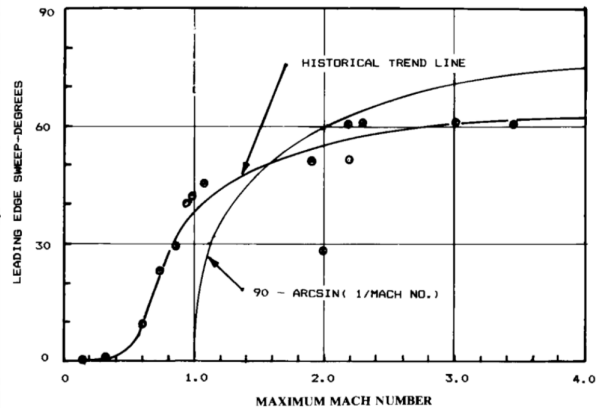


Figure 4: Wing sweep historical trend. [3]

2.6 Taper ratio λ and twist

The taper ratio was one of the parameters, along with the twist, used to optimize the lift distribution along the wing. Starting from historical and published data, at the beginning of the design we were estimating a taper ratio of 0.4 but when the majority of the wing parameters were already defined we started to test our design against a vortex lattice and a panel method algorithms. From the results given by the simulations, a process of optimization started. First of all, we started by simulating a wing with no twist and taper ratio of 0.4. Then we applied small changes to these two parameters, one at a time; if the change in the parameter was such so as to approximate better an elliptical distribution, we increased the magnitude of such change until a new optimum point was found. Following this process the final wing had a taper ratio of 0.2, no twist between $y = 0$ m and $y = 13$ m, and then a linear distribution of twist up to -1° at the tip of the wing. The lift distribution obtained at the end of this process is plotted in Figures 5.

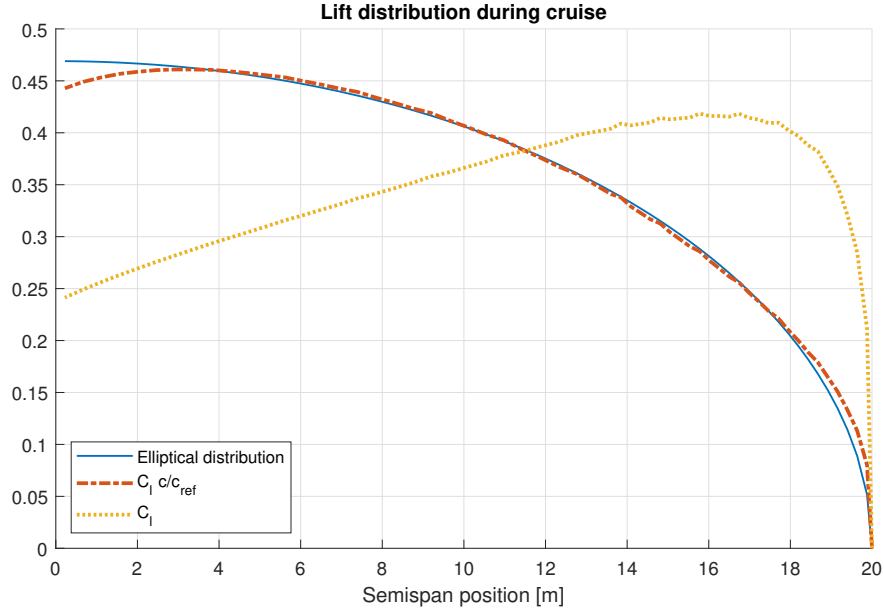


Figure 5: Lift distribution at 0° angle of attack computed with a vortex lattice method. This is the result of several iterations where small changes in the twist distribution and in the taper ratio were used to approximate an elliptical distribution.

2.7 Wing Incidence i_W

The design C_L for our wing is 0.3528 and, during cruise, this is almost perfectly met at a 0° angle of attack (figure 7), therefore, we designed the wing to not have any incidence with respect to the fuselage.

2.8 Dihedral Γ

From historical data we opted to have -2° of dihedral angle as our wing is high mounted and we do not want our plane to be excessively stiff in manoeuvring. This parameter can be defined more accurately by performing an accurate stability analysis of the final aircraft.

2.9 Wing Vertical Location

We opted for an high mounted wing for many different reasons:

- avoid debris and small obstacles while operating the unprepared runway;
- by moving the wing on top of the fuselage we are able to move the cargo bay closer to the ground making ground operations more practical;
- with our design the wing is roughly 6 meters above the ground so crashes with other vehicles or obstacles on the ground are minimised.

2.10 Final design parameters and optimisation

Having defined all the parameters regarding the wing design, we then decided to slightly optimise the pressure distribution at the tip of the wing by rounding the leading edge as it is possible to see in the technical drawings in the appendix.

Table 1: Summary of the wing parameters.

$S_{ref} [m^2]$	209.95	$\Lambda_{c/4}$	25°
$b [m]$	40	λ	0.2
R	7.62	Γ	-2°
Airfoil	NASA SC(2)-0410	i_W	0°
C_L Design	0.3528		

3 Aerodynamic Analysis - Wing Lift

In this section, an aerodynamic analysis of the wing will be performed and the results discussed.

3.1 Clean airfoil aerodynamic analysis

The previously mentioned airfoil (NASA SC(2)-0410) is here simulated against a viscous solver (XFOIL) to better predict the behaviour in the working conditions i.e. cruise and takeoff/landing.

3.1.1 Airfoil lift curve in takeoff/landing

During takeoff and landing the Reynolds number of the flow around the wing is predicted to be 2.195×10^7 and the Mach number is 0.17. Using these parameters, the viscous solver is predicting the lift-line plotted in Figures 6. This prediction is in accordance with the published data in reference [5]. From this graph we can

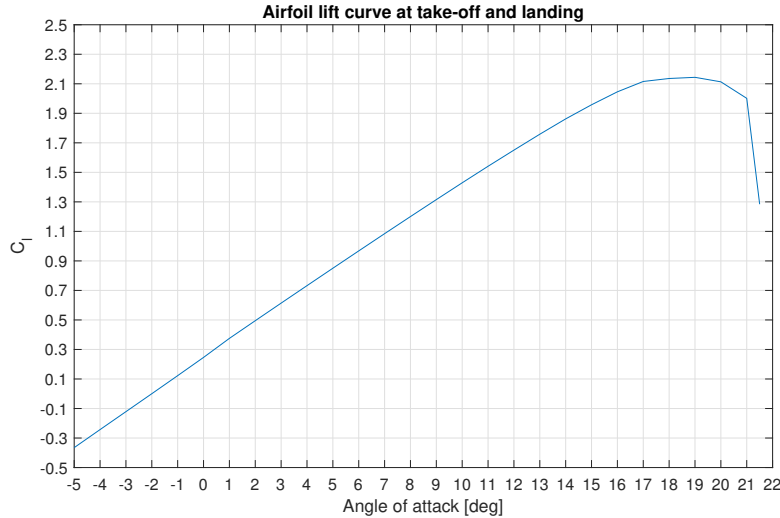


Figure 6: Lift curve of the airfoil computed with XFOIL for $Re = 2.195 \times 10^7$ and $M = 0.17$.

extract the relevant airfoil parameters listed in Table 2.

Table 2: Airfoil lift parameters for $Re = 2.195 \times 10^7$ and $M = 0.17$.

$C_{l\alpha} [1/\text{deg}]$	0.118
C_{lmax}	2.1
C_l at $\alpha = 0^\circ$	0.242

3.1.2 Airfoil lift curve in cruise

During cruise the Reynolds number of the flow around the wing is predicted to be 1.679×10^7 and the Mach number is 0.79. With these parameters, the viscous solver is at its limits of convergence but for the angles of attack relevant for this flight phase, we can still obtain some values. The lift curve for the cruise is reported in Figures 7 and the extrapolated relevant parameters are in Table 3.

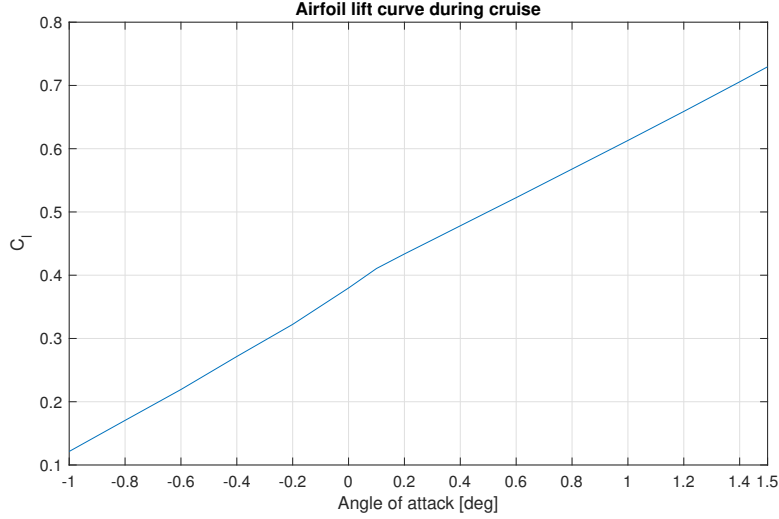


Figure 7: Lift curve of the airfoil computed with XFOIL for $Re = 1.679 \times 10^7$ and $M = 0.79$.

Table 3: Airfoil lift parameters for $Re = 1.679 \times 10^7$ and $M = 0.79$.

$C_{l\alpha}$ [1/deg]	0.240
C_l at $\alpha = 0^\circ$	0.380

3.2 Preliminary high lift devices selection and parameter choice

Our objective in the selection and sizing of the HLD was to meet the C_L requirements for takeoff ($C_L = 2.5$) and for landing ($C_L = 2.7$) which were previously decided. For initial design and estimation of the high lift devices Equation 12.21 and Table 12.2 in Reference [3] were used. A different combination of leading edge and trailing edge devices were considered and in the end, we decided to use Fowler flaps with leading edge slats. In our opinion, this configuration is the one that will ensure we meet our performance constraints by keeping the complexity of the system at the minimum. In applying this equation we used $\frac{S_{flapped}}{S_{ref}} = 0.58$ and $\frac{S_{slatted}}{S_{ref}} = 0.8$.

3.3 Airfoil aerodynamic lift analysis with high lift devices

In this section we try to predict, starting from the airfoil lift curve, the lift characteristic of the wing with the HLD in landing and takeoff configurations. See Table 4 to find all the parameters for the HLD in landing configuration. See Table 5 to find all the parameters for the HLD in takeoff configuration.

Table 4: High lift devices parameters in landing configuration. These parameters were found after various iterations and are the ones that satisfy our minimum requirements.

$\frac{S_{flapped}}{S_{ref}}$	0.58
$\frac{S_{slatted}}{S_{ref}}$	0.80
Flap deflection angle [deg]	35
Slat deflection angle [deg]	20

Table 5: High lift devices parameters in takeoff configuration. These parameters were found after various iterations and are the ones that satisfy our minimum requirements.

$\frac{S_{flapped}}{S_{ref}}$	0.58
$\frac{S_{slatted}}{S_{ref}}$	0.80
Flap deflection angle [deg]	22
Slat deflection angle [deg]	20

3.3.1 Airfoil lift increment due to high lift devices ΔC_l

This is the sectional lift increment at an angle of attack of 0° due to the deployment of the high lift devices computed using the method suggested on page 226 of Reference [7].

Fowler flaps

To determine the airfoil lift increment due to high lift devices given by the Fowler flaps we used Equation 8.6 on page 229 of Reference [7]. See Table 6 to find the parameter relevant to this calculation for the landing case. See Table 7 to find the parameter relevant to this calculation for the takeoff case.

Table 6: Airfoil lift increment due to Fowler flaps in landing configuration.

$C_{l\alpha}$ [1/deg]	0.118
a_δ	0.39
$\frac{c'}{c}$	1.139
δ_f	35°
Resultant ΔC_l	1.834

Table 7: Airfoil lift increment due to Fowler flaps in takeoff configuration.

$C_{l\alpha}$ [1/deg]	0.118
a_δ	0.42
$\frac{c'}{c}$	1.139
δ_f	22°
Resultant ΔC_l	1.245

Leading Edge Slats

For the leading edge slats, the formula used was Equation 8.15 in Reference [7]. See Table 8 to find the parameters relevant to this calculation for both landing and takeoff cases. The two contributions from both the

Table 8: Airfoil lift increment due to leading edge slats in landing configuration.

$C_{l\delta}$	0.02
$\frac{c'}{c}$	1.066
δ_f	20°
Resultant ΔC_l	0.426

leading and trailing edge high lift devices were then added for both landing and takeoff configurations:

- airfoil lift increment due to high lift devices in landing configuration: $\Delta C_l = 2.266$;
- airfoil lift increment due to high lift devices in takeoff configuration: $\Delta C_l = 1.672$.

3.3.2 Airfoil lift curve slope due to flaps $(C_{l\alpha})_\delta$

Generally, the effective wing chord with fully deployed flaps is larger than the clean airfoil chord. Because of this, we used equation 8.17 on page 238 of reference [7] to compute the new lift curve slope. In performing this calculation we assumed the chord with high lift devices to be equal in both landing and takeoff.

Table 9: Airfoil lift curve slope due to high lift devices in landing and takeoff configuration.

$\frac{c'}{c}$	1.206
$C_{l\alpha}$ [1/deg]	0.118
Resultant $(C_{l\alpha})_\delta$ [1/deg]	0.143

3.3.3 Airfoil maximum lift increment due to flaps (ΔC_{lmax})

The airfoil maximum lift increment due to flaps is estimated here.

Fowler flaps

The maximum increment in the lift coefficient due to Fowler flaps was calculated using equation 8.18 on page 239 in reference [7]. For the landing configuration the relevant parameters and results are in Table 10. For the takeoff configuration the relevant parameters and results are in Table 11.

Table 10: Airfoil maximum lift increment due to Fowler flaps in landing configuration.

$k1$	0.80
$k2$	0.98
$k3$	1
$(\Delta C_{lmax})_{base}$	1.22
Resultant (ΔC_{lmax})	0.9565

Table 11: Airfoil maximum lift increment due to Fowler flaps in takeoff configuration.

$k1$	0.80
$k2$	0.82
$k3$	1
$(\Delta C_{lmax})_{base}$	1.22
Resultant (ΔC_{lmax})	0.8003

Leading edge slats

The maximum increment in lift coefficient due to leading edge slats was computed using equation 8.19 on page 239 in reference [7]. In our design, the slats have the same exact chord in both landing and takeoff so we have to compute this calculation only once. The results and parameters used for this calculation are shown in Table 12.

Table 12: Airfoil maximum lift increment due to leading edge slats in landing and takeoff configurations.

$C_{l\delta max}$	1.20
μ_{max}	1.55
δ_f [deg]	20
$\frac{c'}{c}$	1.066
Resultant ΔC_{lmax}	0.692

The two contributions from both leading edge and trailing edge high lift devices were then added for both the landing and takeoff configurations:

- airfoil lift increment due to high lift devices in landing configuration: $\Delta C_{lmax} = 1.649$;
- airfoil lift increment due to high lift devices in takeoff configuration: $\Delta C_{lmax} = 1.492$.

3.3.4 Construction of airfoil lift curve: flaps down

Following the procedure outlined in Figures 8.38 in Reference [7], we are now able to construct the predicted airfoil lift curve for both landing and takeoff configurations. In Figures 8 the landing lift curve is plotted and in Figures 9 the takeoff lift curve is plotted.

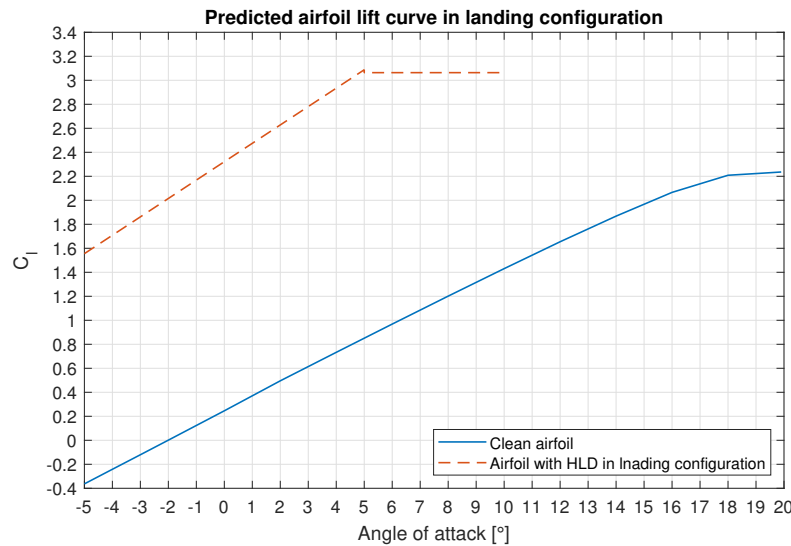


Figure 8: Predicted lift curve of the airfoil with high lift devices in landing configuration.

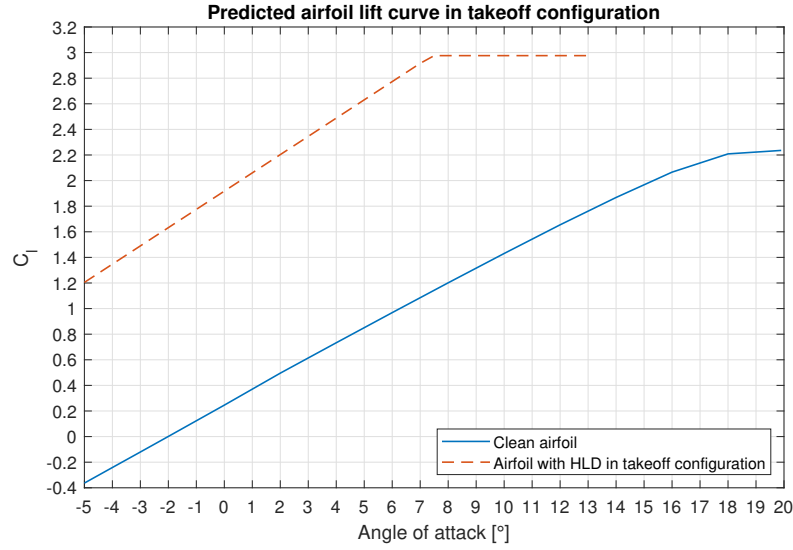


Figure 9: Predicted lift curve of the airfoil with high lift devices in takeoff configuration.

3.4 Clean wing aerodynamic analysis

To obtain reasonable and possibly more accurate data about our wing, the final geometry was simulated with a vortex lattice and a panel code algorithm. The wing was simulated at both Mach 0.17 and 0.79. The results from these simulations were then compared to the published data in reference [5] to check if the results from the simulations were reliable. They resulted to be accurate enough for our initial design but in future stages, a real-life testing will be required to validate such predictions. The prediction of the wing lift curve obtained for a flow of Mach 0.79 can be found in Figures 10.

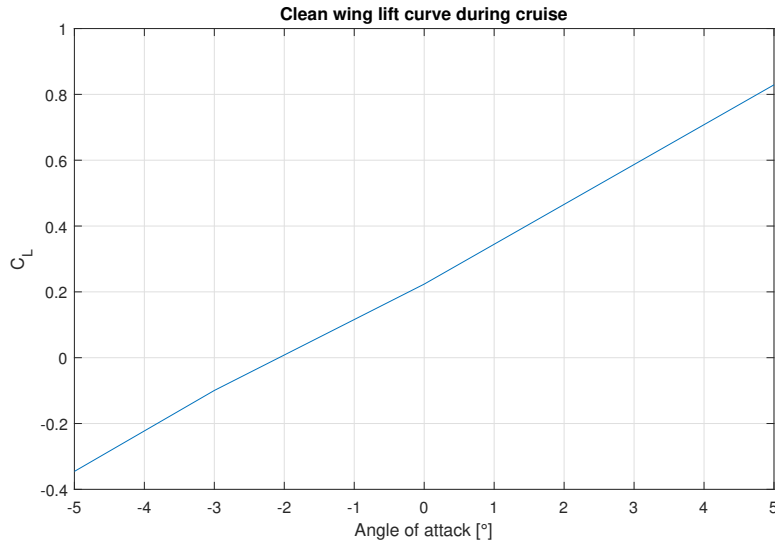


Figure 10: Computed clean wing lift curve at Mach 0.79.

The prediction of the wing lift curve obtained for a flow of Mach 0.17 can be found in Figures 11.

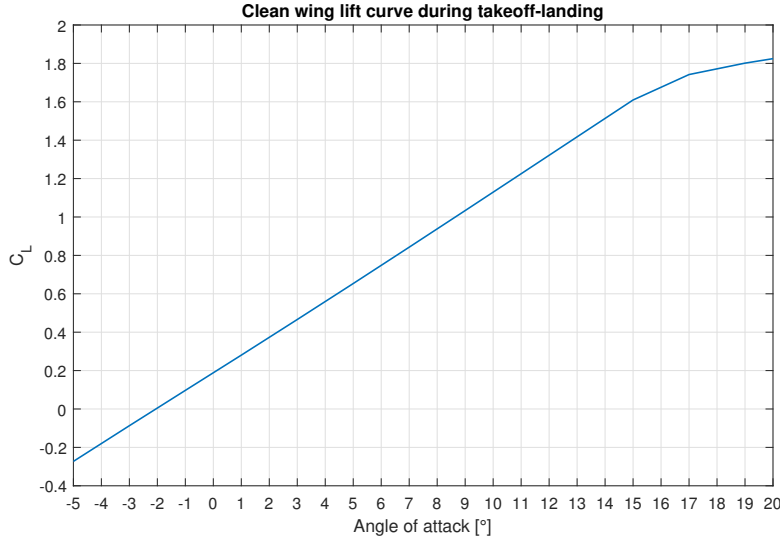


Figure 11: Computed clean wing lift curve at Mach 0.17.

3.5 Wing aerodynamic lift analysis with high lift devices

In this section, we estimate the lift curve of the wing using the procedure described in reference [7] starting from the predictions computed in the previous section.

3.5.1 Wing lift increment due to high lift devices ΔC_{lmax}

To estimate the wing lift increment at zero angle of attack due to trailing edge and leading edge high lift devices, we employed the Equation 8.27 on page 259 in Reference [7]. The parameters and results for the landing and takeoff configurations are in Tables 13 and 14 respectively.

Table 13: Wing lift increment due to high lift devices in landing configuration.

K_b	0.7
$\Delta C_l = \Delta C_{lflap} + \Delta C_{lslat}$	2.266
$C_{L\alpha W}$ [1/deg]	0.088
$C_{l\alpha}$ [1/deg]	0.118
$(\alpha_\delta)_{C_L} / (\alpha_\delta)_{C_l}$	1.05
Resultant ΔC_{lmax}	1.239

Table 14: Wing lift increment due to high lift devices in take-off configuration.

K_b	0.7
$\Delta C_l = \Delta C_{lflap} + \Delta C_{lslat}$	1.672
$C_{L\alpha W}$ [1/deg]	0.088
$C_{l\alpha}$ [1/deg]	0.118
$(\alpha_\delta)_{C_L} / (\alpha_\delta)_{C_l}$	1.05
Resultant ΔC_{lmax}	0.914

3.5.2 Wing lift curve slope due to flaps $(C_{L\alpha W})_\delta$

For a wing equipped with translating high lift devices like the one in our design, the formula to estimate the lift curve slope of the wing with the flaps deployed is given in Equation 8.28 on page 262 in Reference [7]. The parameters and results relative to this calculation are shown in Table 15

Table 15: Wing lift curve slope due to flaps.

$C_{L\alpha W}$	0.088
$\frac{c'}{S}$	1.206
$\frac{S_{wf}}{S}$	0.690
Resultant $(C_{L\alpha W})_\delta$	0.101

3.5.3 Wing maximum lift increment due to flaps ΔC_{LmaxW}

Trailing edge flaps

The maximum wing incremental lift coefficient due to trailing edge flaps is computed using Equation 8.29 on page 262 in Reference [7]. The parameters and results for the landing configuration can be found in Table 16.

The parameters and results for the takeoff configuration can be found in Table 17

Table 16: Wing maximum lift increment due to Fowler flaps in landing configuration.

ΔC_{lmax}	0.957
$\frac{S_{wf}}{S}$	0.580
K_{Δ}	0.869
Resultant contribution to C_{LmaxW}	0.482

Table 17: Wing maximum lift increment due to Fowler flaps in takeoff configuration.

ΔC_{lmax}	0.800
$\frac{S_{wf}}{S}$	0.580
K_{Δ}	0.869
Resultant contribution to C_{LmaxW}	0.403

Leading edge slats

The maximum wing incremental lift coefficient due to leading edge slats is computed with Equation 8.30 on page 262 in Reference [7]. In our case, the maximum wing incremental lift coefficient due to leading edge slats is the same for both landing and takeoff configurations. The parameters and results of this calculation can be found in Table 18.

Table 18: Wing maximum lift increment due to leading edge slats.

$\frac{c_{lef}}{c}$	0.066
$\frac{b_{lef}}{b_e}$	0.850
$\Lambda_{c/4}$ [deg]	25
Resultant contribution to C_{LmaxW}	0.389

The two contributions from both the leading edge and trailing edge high lift devices were then added for both the landing and takeoff configurations:

- wing lift increment due to high lift devices in landing configuration: $\Delta C_{LmaxW} = 0.871$
- wing lift increment due to high lift devices in takeoff configuration: $\Delta C_{LmaxW} = 0.792$

3.5.4 Construction of wing lift curve: flaps down

Following the process described in Figures 8.58 in on page 264 of reference [7], we can obtain the predicted lift line curve for the wing in landing and takeoff configuration. These plots can be found in Figures 12 and 13.

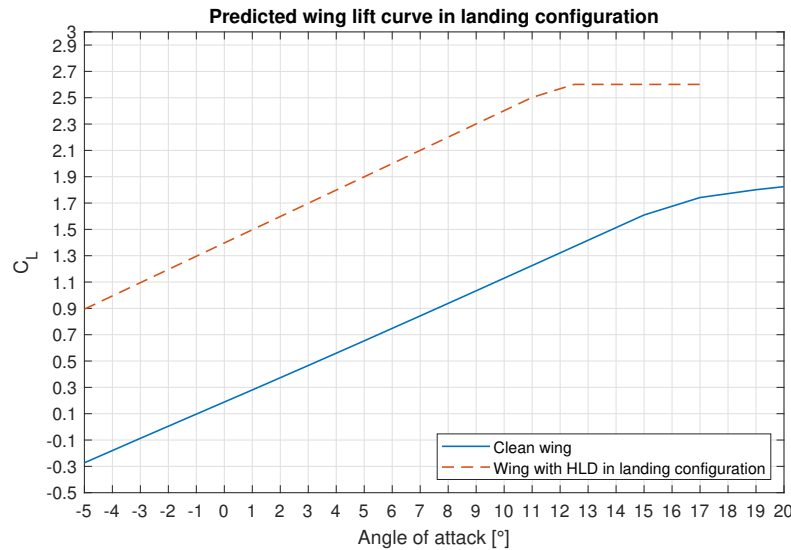


Figure 12: Predicted lift curve of the wing with high lift devices in landing configuration.

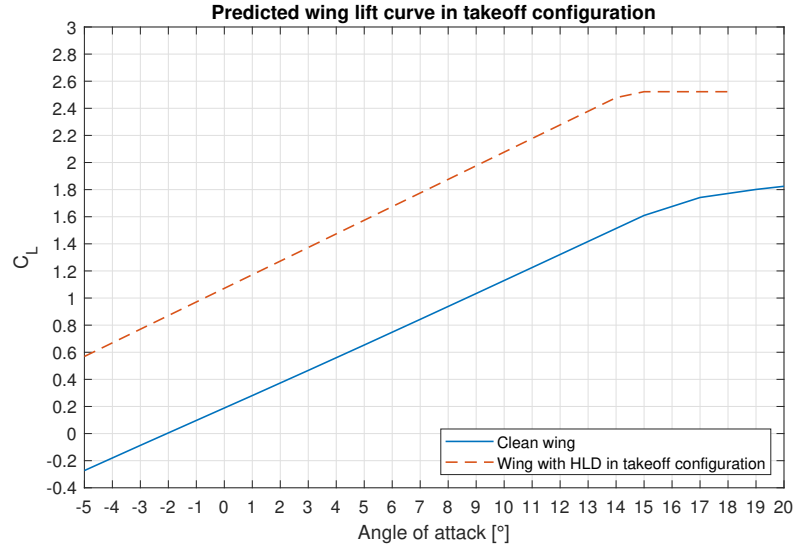


Figure 13: Predicted lift curve of the wing with high lift devices in takeoff configuration.

3.5.5 Construction of wing lift curve: flaps down

4 Tailplane sizing and design

4.1 Overview

The tail can be divided into the horizontal and vertical tailplane: combined together, these have 3 primary functions: (i) longitudinal and directional trim (ii) longitudinal and directional stability and (iii) longitudinal and directional control in critical conditions such as nosewheel lift-off, low speed flight with flaps (horizontal tail) and engine-out at low altitude, maximum roll rate, recovery from a spin (vertical tail); they must therefore be sized accordingly. The final parameters are tabulated in Table 20 .

4.2 Horizontal tailplane

The primary function of the horizontal tail is to counteract the various moments generated at different points in the aircraft (for example the zero-lift pitching moment of the fuselage, longitudinal moment of the aircraft's wing about the CG and the engine thrust longitudinal moment) and provide longitudinal stability and trim for the major flight phases such as takeoff, cruise and landing. More often than not, it produces negative lift to do so, and as such the tail setting angle i_h is also negative. The first step is to select the configuration; despite 70% of the aircraft in service using a conventional tail [3], we chose an aft T-tail, since it is used by similar military aircraft (A400M, C-130), which facilitates the analysis in the initial design stage (contrary to a canard) and offers the following advantages [8]:

- It is situated out of the region of the wing wake, wing downwash and engine gasses, meaning a higher efficiency and a safer structure. It also means a decreased area, and less tail vibrations leading to lower fatigue problems and an increased lifetime.
- The end-plate effect leads to a reduced vertical tailplane size (area).

However, the main disadvantage is deep stall. This is a condition where the wake of the main wing impinges on the tail surface, rendering it almost ineffective. To counteract this the horizontal tailplane must be vertically positioned outside of the wing's turbulent wake, according to Figures 14. Eventually it was decided that $\frac{z_h - z_w}{c} = 1.5$.

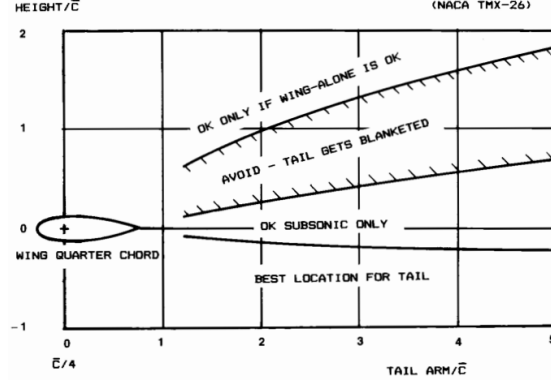


Figure 14: Horizontal tail positioning [3]

4.2.1 Area

The planform area S_H of the horizontal tailplane is initially determined using the tail volume coefficient, \bar{V}_H :

$$\bar{V}_H = \frac{l_H S_H}{c_w S_w} \quad (4)$$

where l_H is the distance between the wing and the tailplane aerodynamic centre. As l_H is maximised, the tailplane area S_H is minimized. Initially, empirical data [3] suggests that l_H should be 55% of the fuselage length, for an aircraft with its engines on the wing, yielding $l_H = 21.45\text{m}$. Furthermore, for an aircraft with a T-tail, \bar{V}_H must be reduced by 5% due to the clean air seen by the horizontal tail. Additionally, since this aircraft uses a computerized flight control system, S_H is reduced by 10% (assuming as a first approximation that all trim, engine-out and nosewheel lift-off requirements are met [3]). With the above values, $S_H = 44.37\text{m}^2$ and $\bar{V}_H = 0.94$ (see Table 20). However, this area was deemed too low since the aircraft was not longitudinally statically stable (see section 7), and eventually it was increased to $S_H = 75\text{m}^2$.

4.2.2 Airfoil selection

The airfoil must have the largest possible lift curve slope and be used at a considerably wide range of angles of attack. Due to the fact that the CG moves during flight, the tail must produce sometimes positive and sometimes negative lift. As a consequence, a symmetric airfoil section should be used. In our case, however, since the wing's aerodynamic centre is always aft of the CG, an inverted airfoil is used since it must generate negative lift throughout the flight. Additionally, compressibility effects must be minimized. This is done in two ways. First of all, by selecting a supercritical airfoil. Secondly, $C_{L,H}$ must be lower than $C_{L,w}$, which means that the Mach number seen by the horizontal tailplane must be lower than that of the wing. This can be done with an airfoil about 2% MAC thinner than the wing's. The NASA SC(2)-0406 was eventually selected. Reference [8] states that the airfoil's 3D lift curve slope (shown in Table 19) is determined using:

$$C_{La} = \frac{2\pi \mathcal{R}_H \frac{S_{exp}}{S_{ref}} F}{2 + \sqrt{4 + \frac{\mathcal{R}_H^2 \beta^2}{\eta_{airf}^2} (1 + \tan\left(\frac{\Lambda_{max}}{\beta^2}\right)^2}} \quad (5)$$

where $\beta = \sqrt{1 - M^2}$, $\eta_{airf} \approx 0.95$, $F = 1$ is the fuselage spillover lift factor for the tail and Λ_{max} is the sweep at the airfoil's location of maximum thickness. C_{La} is shown in Table 19. Finally, the horizontal stabilizer should stall after the wing, and should therefore have a higher α_{max} than the main wing to ensure stall recovery.

Table 19: The horizontal tailplane's 3D lift curve slope.

Configuration	$\frac{dC_L}{d\alpha}$ (rad ⁻¹)
Cruise	4.70
Takeoff, point 1	0.22
Takeoff, point 5	0.68
Landing, point 4	1.65
Landing, point 8	2.18

4.2.3 Sweep $\Lambda_{\frac{c}{4}}$

The main benefit of adding sweep is that it increases the critical Mach number, M_{crit} , delaying the onset of compressibility effects. As such, wave drag is reduced, translating into a more effective horizontal stabilizer even at high speeds. Furthermore, sweep increases the distance of the tail's aerodynamic centre from the aircraft datum, leading to a higher moment arm about the CG, increasing the longitudinal static stability of the aircraft. As an initial estimate, $+5^\circ$ were added to the wing sweep in order to determine the horizontal tailplane sweep [3]. This also ensures the tail stalls after the wing. Consequently, $\Lambda_{\frac{c}{4}} = 30^\circ$.

4.2.4 Aspect ratio

An important requirement for stall recovery is that the tail must stall after the main wing so as to have effective elevators. As a consequence, a lower aspect ratio must be selected for the horizontal tailplane. Based on [9], this ranges from 1.8 to 6.9 for military transport aircraft. Finally, $\mathcal{R} = 6.9$ was selected.

4.2.5 Taper ratio λ

The main drivers behind this choice are structural considerations, namely to lower the tail weight [8]. Typical values for similar aircraft [9] are between 0.31 and 0.8. Thus, the lowest value of $\lambda = 0.31$ was chosen.

4.2.6 Dihedral angle

As an initial estimate, the dihedral angle for the tail was set to be the same as the main wing's, namely -2° .

4.2.7 Twist

Twist is an aerodynamic feature allowing lift redistribution along the wing. Its purpose is to ensure that the wingtip is the last part of the wing to stall, by decreasing the effective angle of attack at the tip (wash-out). Consequently, it can be crucial in allowing the pilot to both be aware of and recover from a stall. As a first iteration, 0° of twist were used, a decision which will be revised at a later stage when more of the aircraft's stall characteristics are known.

4.3 Vertical tailplane

The vertical tailplane is mainly responsible for maintaining directional stability and trim. Since most airplanes are symmetric about their xz plane, the former is usually satisfied in normal flight conditions. In cases of asymmetric thrust, crosswinds and spin, it must generate a sufficient yawing moment to counteract these states.

4.3.1 Area

The area of the vertical tailplane is initially determined using the tail volume coefficient, V_V :

$$\bar{V}_V = \frac{l_V S_V}{b_w S_w} \quad (6)$$

where l_v is the distance between the vertical tail and wing aerodynamic centre. Increasing this will make the aircraft more directionally stable. As a first iteration, it is set equal to the horizontal tail's moment arm l_H (obviously this is wrong especially if the horizontal tailplane has sweep, however it is a good approximation for a first iteration). Furthermore, due to the end plate effect in a T-tail, \bar{V}_V should also be reduced by 5%. The initial tail area is $S_v = 26.86m^2$ (see Table 20). This is relatively small, and two approaches to solve this problem would be to employ either a ventral or a dorsal fin in a further iteration.

4.3.2 Airfoil selection

The vertical tailplane generates the vertical lift coefficient C_{Lv} , and must also ensure symmetry about the xz plane; as a consequence, it must be symmetric. Furthermore, it must be clean of compressibility effects. Since a T-tail is used, the vertical tail must sustain the weight of the horizontal one, therefore a thicker airfoil section must be used. The NASA SC(2)-0012 was the final decision.

4.3.3 Aspect ratio \mathcal{R}_v

The vertical tail aspect ratio for military transport aircraft lies in the range $0.9 < \mathcal{R}_v < 1.9$ [9]. The final decision was to use the highest aspect ratio possible, since it offers two important advantages [8]: first of all, a higher aspect ratio increases the vertical tail arm l_v resulting in a greater yawing moment arm and consequently higher directional control. Secondly, increasing \mathcal{R}_v increases the vertical tailplane's height, leading to the horizontal tailplane being outside of the wing's wake, allowing the pilot to prevent a deep or even a super stall. As such, $\mathcal{R}_v = 1.9$.

4.3.4 Taper ratio λ_v

Its main purpose is two-fold, namely: (i) reduce the bending stress on the vertical tail's root and (ii) ensure sweep can be used on the vertical tail [8]. For military transport aircraft, $0.28 < \lambda_v < 1.0$ [9]. In the end, $\lambda_v = 0.28$ was selected as an initial estimate.

4.3.5 Sweep $\Lambda_{\frac{c}{4}}$

Sweep decreases wave drag in high-speed subsonic flight, in addition to offering increased directional control of the aircraft [8]. Data for the same type of aircraft [9] led to $\Lambda_{\frac{c}{4}} = 37^\circ$.

Table 20: Summary of the main tailplane parameters

Parameter	Horizontal	Vertical
\bar{V}	0.94	0.076
\mathcal{R}	6.9	1.9
S (m^2)	75	26.86
\bar{c} (m)	3.30	3.96
c_{root}/c_{tip} (m)	4/1.24	14.29/4
$\Lambda_{\frac{c}{4}} (^\circ)$	30	37
Airfoil	NASA SC(2)-0406	NASA SC(2)-0012
$\frac{t}{c}$	6 %	12%
$C_{l,\alpha}$ (rad^{-1})	1.04	1.04
$C_{L,\alpha}$ (rad^{-1})	5.73	5.73
α_0 ($^\circ$)	0	0
λ	0.31	0.28
Dihedral ($^\circ$)	-2	N/A
i ($^\circ$)	-1	0

5 Power plant selection (do not mark)

In selecting a power plant system for a semi-prepared runway capable cargo aircraft emphasis was put in redundancy of systems, long range capability and low fuel consumption to reduce both operating costs and takeoff weight. High bypass turbofan engines therefore created the pool of engines from which selection was made.

5.1 Selection

Given that the typical mission profile flown includes serving semi-prepared runways a four engine design was preferred for redundancy purposes. Since this kind of aircraft could also be called upon for long range missions or it might be necessary to position the aircraft in a distant base only extended operations (henceforth ETOPS) certifiable engines and Auxiliary power units (APU) were considered. The minimum total required thrust, determined from the constraint diagram in 1 and losses due installation, is of 338 kN. Dividing the required

thrust by the number of engines led to a value of 84.4 kN. Engines that both met this thrust value and were ETOPS certifiable were lower bypass ratio engines optimised for Mach numbers greater than our cruise speed of Mach 0.79. Rubber engine sizing of a higher bypass ratio optimised for lower speeds was therefore preferred. The engine selected to perform the rubber engine sizing was the Pratt Whitney PW1122G, the smallest of the ETOPS certifiable PW1100G family, it entered service in 2016.

5.2 Integration

5.2.1 Inlet

The inlet at the front of the engine was designed to reduce the mach number of the incoming flow to values of between 0.4 and 0.5 at cruise condition and achieve a pressure recovery of above 96%. The capture area, tabulated in table 22 and sized based on mass flow rate needed at different conditions throughout the flight, is of 1.83 m^2 . In order to minimise flow separation at the high angles of attack needed to perform takeoffs at short runways a large lip radius was chosen; 9% for the inner lip radius and 4% for the outer lip. Besides minimising distortion due to high angles of attack, it also minimises distortion due to sideslip or cross wind landings, allowing it to land safely on runways which, due to their improvised nature or other constraints, might not always line up with the prevailing winds.

5.2.2 Nozzle

A fixed nozzle was chosen due to the speeds the aircraft would fly at. The reduced weight and maintenance of such a design outweigh the minor losses in performance. Following from [3] an exhaust area of 1.1 m^2 was selected. This is tabulated in table 22

5.2.3 Thrust reverser

Thrust reversers installed on this aircraft have multiple benefits. In landing, thrust reversers reduce the ground roll by 1/3, allowing for more efficient wing loadings to be achieved. Once on the ground, especially when operating from semi-prepared strips, thrust reversers allow the aircraft to powerback on its own. This might be necessary to use the full runway length to takeoff or just convenient during pushback. On the ground thrust reversers that direct the flow up also allow the engines to keep running while loading the aircraft. This might be done in order to power aircraft systems or just to reduce the time an aircraft is on the ground.

5.3 Dimensions

Table 21: Engine parameters, scale factor 0.78

Parameter	PW1122G	Rubber engine
Thrust	108 kN	84.4 kN
Mass	2858 kg	2184 kg
Length	3.401 m	3.084 m
Diameter	2.22 m	1.97 m

Table 22: Summary of chosen engine area values

Fan area	3.87 m^2
Capture area A_c	3.12 m^2
Nozzle Area	1.87 m^2

5.4 Auxiliary Power Unit

The APS 3200 Auxiliary Power Unit was chosen based on power provided: 90 kVA, enough to power the hydraulics on board the aircraft and start up its engines; and its ETOPS certifiability. Its dimensions are tabulated in table 23

Table 23: Auxiliary Power Unit dimensions and mass

Mass	140 kg
Length	1247 mm
Width	863 mm
Height	757 mm

6 Control surface design

The primary control surfaces of the aircraft are the ailerons, elevator and rudder, which control the aircraft in roll, pitch and yaw accordingly.

6.1 Ailerons

In industry, this process would involve a significant amount of dynamic analysis of control effectiveness. However, for initial design purposes, the ailerons can be sized using Figures 15, and they are initially given the maximum deflection allowable [8]. Their size is constrained by the longitudinal extension of the flaps and spoilers along the wing. Historically, ailerons extend from 50 to 90% of the wing's semi-span. Due to the flaps extending all the way to 66% of the wing semi-span, ailerons in this aircraft extend from 66 to 96% of the wing semi-span.

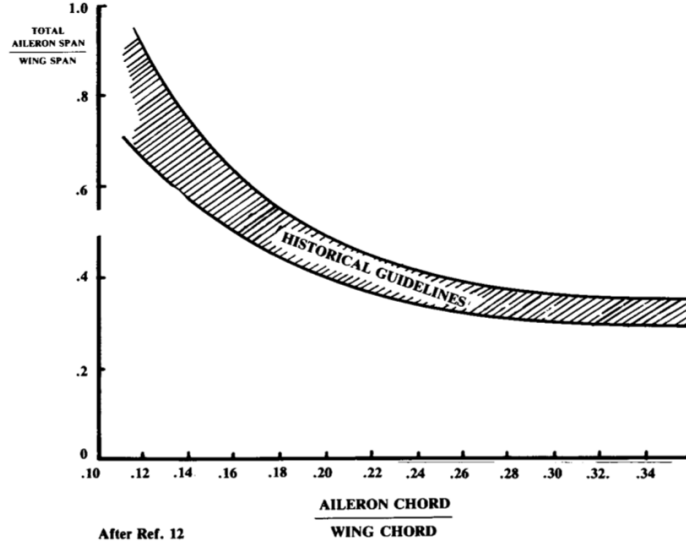


Figure 15: Empirical aileron sizing curve [3]

Aileron to wing span ratio was selected to be 0.3, resulting in the same ratio of aileron to wing chord. This agrees well with the value of similar-sized aircraft like the C-130 (chord ratio=0.29). A phenomenon countered by high-speed aircraft is aileron reversal: this is when the loads on the deflected aileron are so great that the wing itself is twisted [3]. The solution traditionally employed is the use of inboard ailerons and/or spoilers, in some cases even aerodynamic balancing. Nevertheless, such an analysis comes at a later stage and only outboard ailerons were used.

6.2 Elevator

The first parameter to be determined is the elevator's chord length, c_e , done by consulting the values of similar type of aircraft. Using [10], for a jet transport aircraft (the closest to our case), $\frac{c_e}{\bar{c}} = 0.25$, where \bar{c} is the wing's MAC. In Table 24, the maximum elevator deflection for similar type of aircraft was chosen as a first iteration, according to [8]. Since the aircraft could operate in war zones, the pilot should be given full control and manoeuvrability to avoid, for instance anti-aircraft missiles. Furthermore, it is assumed that the elevator begins at the tip and extends to 90% of the horizontal tailplane's span, since this is historically the case [3].

6.3 Rudder

The rudder is responsible for ensuring the directional-lateral stability of the aircraft. Its deflection must create a yawing moment large enough to bring the aircraft back to its equilibrium state, especially in the most critical flight conditions such as: asymmetric thrust (one or more engines inoperative), a crosswind landing/takeoff, and spin recovery. For the first case, the pilot is given a deflection of $\pm 35^\circ$ (value for the C-130 from [9]), which should be able to counteract the moment generated from the excess thrust from one side of the aircraft, while assuring that the pilot can "crab" the aircraft in the second case. In the third case, when a spin occurs, the aircraft rotates about its vertical axis and simultaneously falls vertically down (the main wing is fully stalled), at a large sideslip angle [3]. The first step to recover is to eliminate the rotation, using the rudder. The deflection angles chosen previously were deemed to be sufficient as a first iteration. Finally, the rudder is initially set to extend from 20 to 90% of the semi-span of the vertical tailplane, since this is within the allowed empirical range [3]. For a jet transport aircraft, $\frac{c_R}{c_V} = 0.32$.

6.4 Summary of control surface parameters

Table 24: Summary of control surface design characteristics

	Aileron	Elevator	Rudder
Area ratio	0.05	0.25	0.17
Chord ratio	0.30	0.25	0.32
Position (% semi-span)	66-96	0-90% of span	20-90%
Deflection (δ)	-25/+20°	-20/+20 °	$\pm 35^\circ$

7 Static stability and trim analysis

Static stability refers to the aircraft's immediate tendency to return to its equilibrium state following a perturbation, and is divided into: (i) longitudinal (in pitch), (ii) lateral (in roll) and (iii) directional (in yaw).

7.0.1 Longitudinal static stability

A longitudinally statically stable airplane produces a sufficient pitching moment that counteracts any perturbations in pitch. The condition for such stability is thus $\frac{\partial C_M}{\partial \alpha} < 0$. Initially, power-off, longitudinal stability must be considered:

$$\frac{\partial C_{M,cg}}{\partial \alpha} = -C_{L\alpha,w}(\bar{x}_w - \bar{x}_{cg}) + C_{M,\alpha f} - \eta_H C_{L\alpha,H} \left(1 - \frac{d\epsilon}{d\alpha}\right) \frac{S_H}{S_w} (\bar{x}_H - \bar{x}_{cg}) \quad (7)$$

where $\eta_H \approx 1$ (for a t-tail) is the tailplane efficiency factor, $C_{M,\alpha f} = \frac{K_f L_f w_f^2}{\bar{c} S_w} \approx 0.96$ with $K_f \approx 0.78$ [11], x_w, x_H are the aerodynamic centres of the wing and tail respectively (measured from the aircraft datum), $\frac{d\epsilon}{d\alpha} = 0.84$ for cruise and $C_{L\alpha,w}, C_{L\alpha,H}$ are the 3D lift curve slopes of the wing and horizontal tail respectively. Equation 7 highlights a very importance fact: the static stability is dependent upon the CG, x_w, x_H and S_H . These three parameters are interlinked, meaning that a change in the position of the wing or the tailplane will influence the CG. Consequently, the stability engineer must work closely with weight and balance to determine where the CG will lie in each loading configuration. Then, depending on whether the aircraft is statically stable or not, the wing position can be shifted, and the CG should be computed again, along with the new static stability analysis. The tailplane area and position also influence the said analysis. Increasing S_H and/or x_H will lead to a more effective tailplane. However, the CG must be then re-computed to account for the tailplane's added weight, which will again mean that a new static stability analysis needs to be performed. Our team decided to initially keep l_H (since it has its maximum value), fixed, place the horizontal tail as far aft as possible (including by adding the maximum amount of sweep possible) and try to move the wing to a position that would yield reasonable static margins. Eventually, $x_w = 18.76$ m.

Setting $\frac{\partial C_{M,cg}}{\partial \alpha} = 0$

$$\bar{x}_{np} = \frac{C_{L\alpha,w} \bar{x}_w - C_{M\alpha,f} + \eta_h C_{L\alpha,h} \left(1 - \frac{d\epsilon}{d\alpha}\right) \frac{S_H}{S_w} \bar{x}_h}{C_{L\alpha,w} + \eta_h C_{L\alpha,h} \left(1 - \frac{d\epsilon}{d\alpha}\right) \frac{S_H}{S_w}} \quad (8)$$

the neutral point can be computed. This is defined as the aft most position of the CG for the aircraft to remain longitudinally statically stable, in effect it is the airplane's aerodynamic centre, where any lift resulting from a change in the angle of attack will act through. Of course, the aircraft must be stable for all configurations: for the pallets, troops, helicopter and empty payload loading conditions. The second step is to calculate the power-off static margin, K_{off} :

$$K_{off} = \bar{x}_{np} - \bar{x}_{cg} \quad (9)$$

Then, the power-on static margin is empirically given as $K_{on} = K_{off} - 0.02$ for transport aircraft [11] and has to be positive for longitudinal static stability. It is usually between 4-7% and never above 20% [?]. The case with the helicopter is the one where the CG is at the most aft position, and should therefore receive the most attention. Table 25 shows the power-off and power-on static margins for the three different loading configurations; it highlights three facts. First of all, the aircraft is very stable when the pallets are loaded,

which is desirable; however the aircraft is also more "sluggish" and stiffer to control, increasing pilot workload. Secondly, that the helicopter is indeed the configuration for which the lowest K_{on} is exhibited (in fact it is unstable for landing, see Figures 19). Nevertheless, and since this is a military cargo aircraft, the position of the CG can be changed by the loadmasters during the flight, should any issues arise. Finally, the aircraft exhibits an excellent balance between static stability and control effectiveness when it carries the troops. Consequently, the aircraft is longitudinally statically stable.

Table 25: Static stability analysis for different loading configurations

Loading	\bar{x}_{cg}	\bar{x}_{np}	K_{off}	K_{on}
Pallets	2.87	3.07	19.7%	17.7%
Troops	3.00	3.12	12%	10%
Helicopter	3.07	3.12	5.1%	3.1%

7.0.2 Directional-Lateral static stability

The purpose is to determine whether the aircraft can counteract the generated yawing (N) and rolling (L) moments from a perturbation in sideslip angle β . The conditions for directional-lateral stability are $\frac{dN}{d\beta} \geq 0$ and $\frac{dL}{d\beta} \geq 0$. The vertical tailplane must be sized accordingly. Since this is just a first iteration, it is assumed the aircraft is initially laterally stable, an assumption which will be revised at a later iteration.

7.1 Trim

The last step is to determine that tail setting angle, i_H , for which the aircraft is trimmed. This is done by plotting $C_{m,cg}$ vs C_L for different tail-setting angles:

$$C_{M,cg} = -C_{L,w}(\bar{x}_w - \bar{x}_{cg}) + C_{M0,w} + C_{M,af}\alpha - \eta_H C_{L,H} \frac{S_H}{S_w} (\bar{x}_H - \bar{x}_{cg}) + \frac{Z_T T}{q S_w \bar{c}} \quad (10)$$

, where Z_T is the thrust moment arm, T is the thrust at the respective leg of the flight, q is the dynamic pressure and \bar{c} is the wing's MAC. Figures 16, 17, 18 show the trim plots the helicopter, pallet and troop loading cases for cruise at $M=0.79$. Figures 19, 20, 21 show the same trim plots for landing. In all cruise cases, $C_{L,des} \approx 0.5$. Consequently, the final selection was $i_H = -1^\circ$. Note that trimming the takeoff and landing is more tricky. Unfortunately, our team was not able to find a good compromise between an x_w value and reasonable static margins, within the limits specified above; consequently, takeoff plots are not included because it would not make sense to chose i_H using an unstable configuration. In the landing case, and as specified previously, the helicopter configuration is not statically stable, a situation that can be fixed by the loadmasters in flight. However, instability is associated with higher manoeuvrability; in semi-prepared airfields, in the middle of enemy territory, this can be crucial for the safety of the cargo and crew. Furthermore, since we are using computerized flight control systems, the computer can ensure that the plane will be stable even with slightly negative static margins. Nevertheless, trim will be revised at a later iteration.

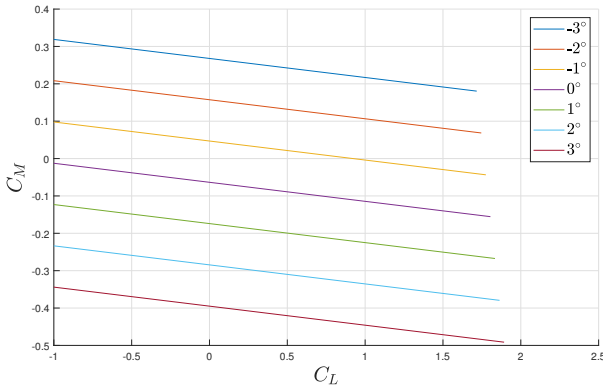


Figure 16: i_H , with the helicopter, for cruise

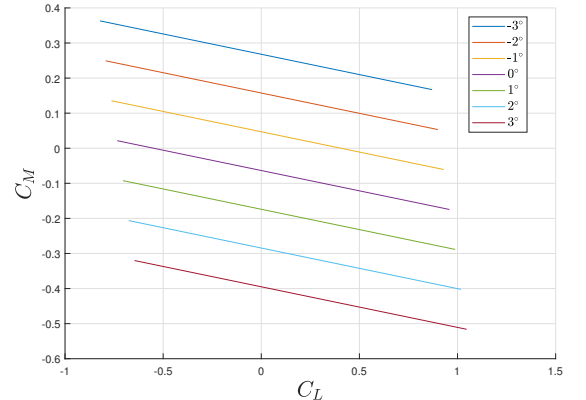


Figure 17: i_H , with the pallets, for cruise

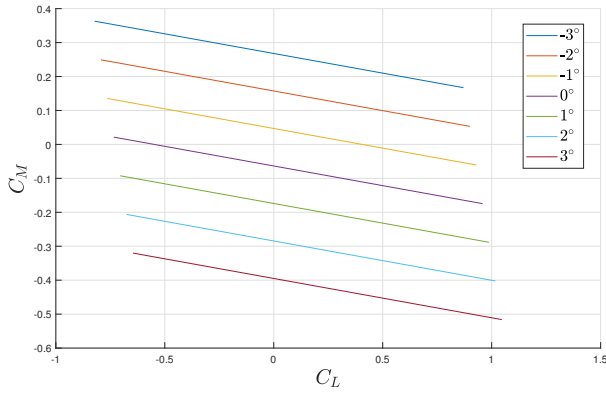


Figure 18: i_H , with the troops, for cruise

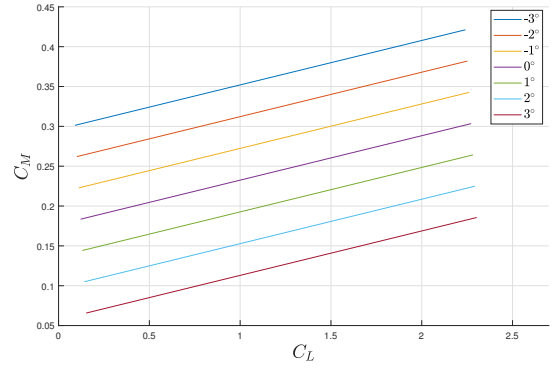


Figure 19: i_H , with the helicopter, for landing

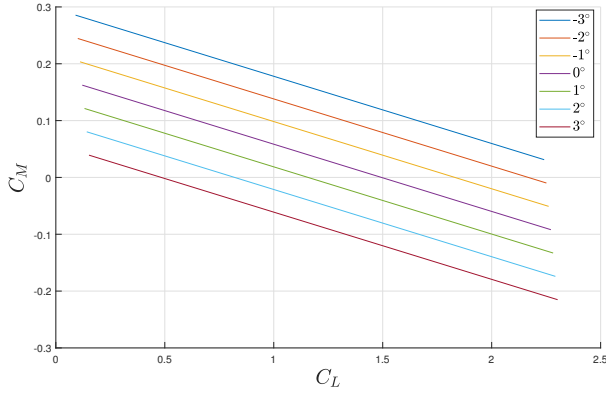


Figure 20: i_H , with the troops, for landing

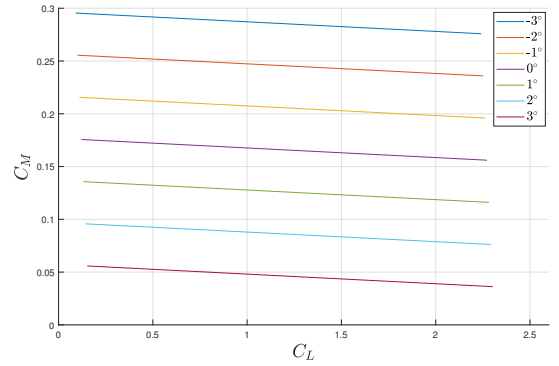


Figure 21: i_H , with the pallets, for landing

8 Fuselage design & sizing

Figure 22 presents the side view and the top view of the fuselage with naming of each fuselage section. Unless stated otherwise, all dimensions shown in this Section are in meters.

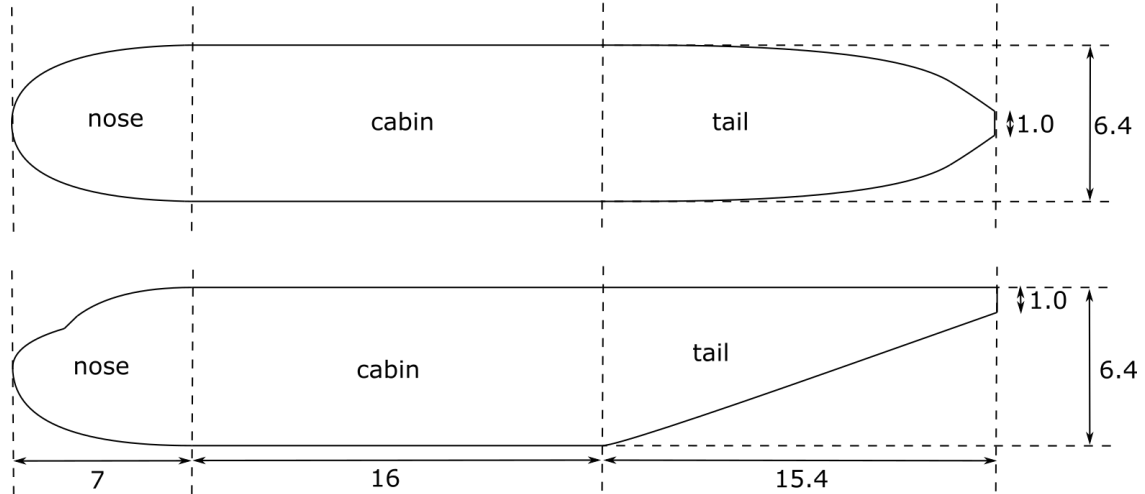


Figure 22: Top and side view of the fuselage

8.1 Fuselage cabin

The design of the fuselage cabin was governed by the dimensions and the layout of the possible loads. In addition to 8 Standard pallets and the Merlin helicopter, the fuselage had to be able to hold 130 fully equipped troops using palletized or sidewall seating which would agree with seating requirements set by FAR 25. Using

trial and error, a final configuration of payload as well as first rough fuselage section and length were reached. The fuselage section was then optimized using method presented in Section 8.2. The fuselage cross-section is presented in Figure 23. It is composed of four conic curves. More details about the geometry of the conics can be found in Figure 24.

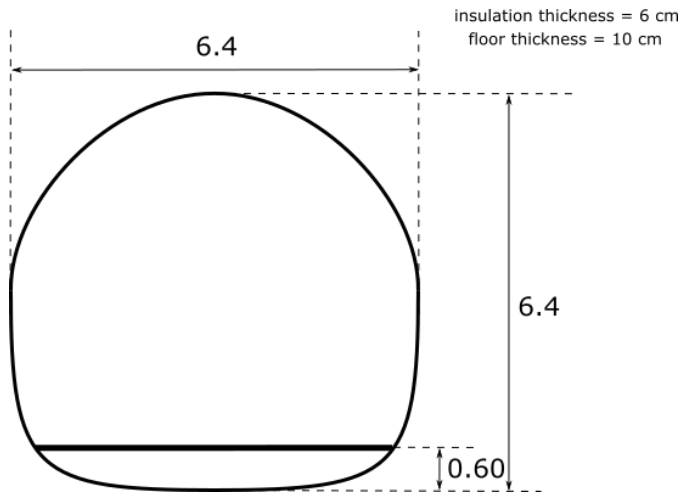


Figure 23: Fuselage cross-section

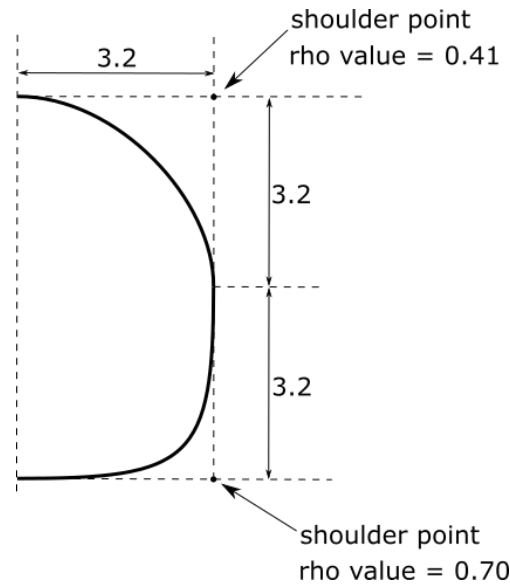
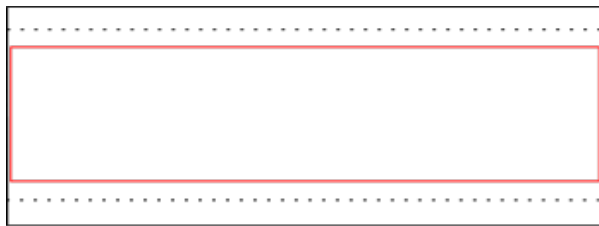


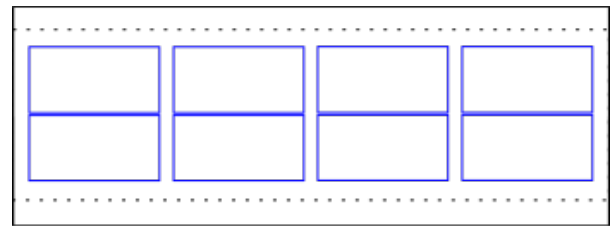
Figure 24: Conic curves geometry (lateral symmetry)

The floor plan for three cases (helicopter, pallets, troops) is presented in Figures 25, 26 and 27.



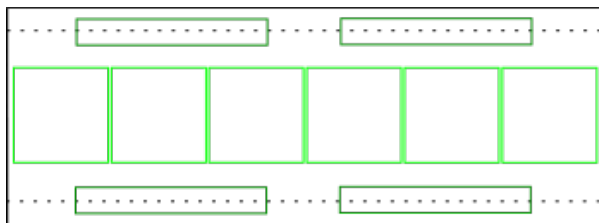
..... cargo floor
 — cabin outline
 — helicopter outline

Figure 25: Cabin layout for helicopter



..... cargo floor
 — cabin outline
 — pallet outline

Figure 26: Cabin layout for pallets



..... cargo floor
 — cabin outline
 — palletized seating outline
 — side seating outline

Figure 27: Cabin layout for troops

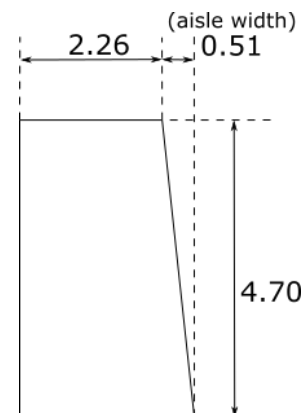


Figure 28: Trapezoid dictating fuselage cross-section

8.2 Fuselage section optimization

The purpose of the optimization was to find the perfect balance between the additional weight due to harder pressurization of non-circular cross section and the drag savings due to the lower cross sectional area and the decreased wetted area. The additional considerations for the section shape were also: proximity to the ground, space for system layout and structural safety. The fuselage section was composed of two conic curves (Figure 24). The section had to encompass a trapezoid of height and bases determined by helicopter dimensions (see Section 8.3). The algorithm varied the parameters of the bottom curve (the length between the lowest point of the fuselage and the cargo floor), and for each iteration it calculated the normalized skin weight, normalized cross-sectional area and normalized arc length. The first ratio was multiplied by weight of the fuselage and divided by L/D ratio to obtain drag penalty due to higher pressurization costs. The latter two ratios were multiplied by each other and by zero lift drag at cruising conditions (look Section 11.1) to obtain drag savings due to the decreased cross sectional area and fuselage wetted area. The results of the optimization are presented in Figures 29 and 30. The parasitic drag is much more significant than the weight penalty. However, due to the other considerations mentioned in the next section, the length between cargo floor and the lowest fuselage point was chosen to be 0.6 m. Furthermore, the conics were adjusted so that the all the distances between conic curves ends and shoulder points were the same.

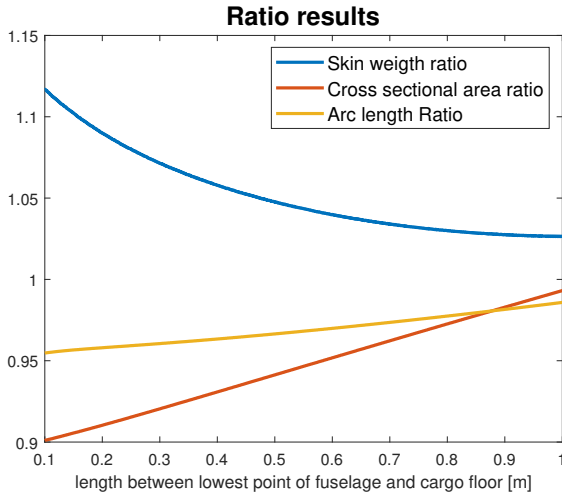


Figure 29: Relation between conic curve parameter and ratios

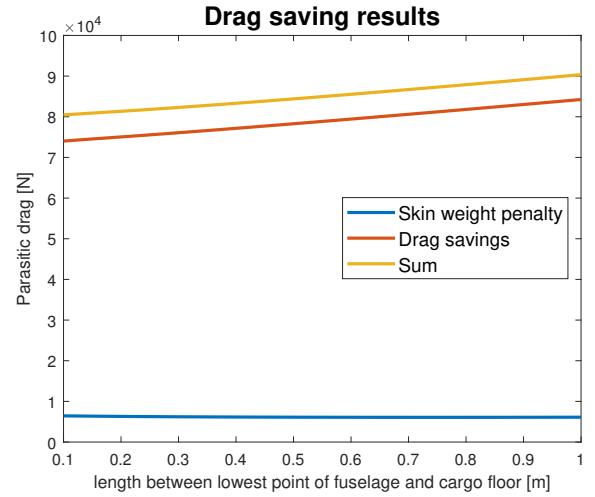


Figure 30: Relation between conic curve parameter and drag penalty

Additional notes on fuselage section optimization

Many of the parameters and relations necessary for the optimization are unknown and had to be approximated. The relation between radius of curvature and skin thickness was taken as a linear function with saturation threshold. The coefficient of linearity was taken so that for a circular cross sectional area, the thickness is equal to 3 mm and the threshold value was taken to be 6 mm (twice that for a circular cross-section). This assumption is very inaccurate. To alleviate the effects of this error, the calculated ratios were normalized. Furthermore, usage of rule could further reduce the drag of the fuselage. However, due to the dimensions of the helicopter, the successful implementation of the area rule could be difficult.

8.3 Helicopter considerations

The helicopter was the largest of the payloads. Its length governed the length of the fuselage. The height and the width of the helicopter dictated the dimensions of the trapezoid that the fuselage section had to encompass. The height of the trapezoid was obtained considering the fact that the helicopter had not only to fit inside but also to be loaded inside. Using initial estimates of the fuselage upsweep angle and the APU dimensions, the height of the trapezoid was estimated geometrically using CAD. The top width of the trapezoid was governed only by the helicopter width. The bottom of the trapezoid had to be wide enough to allow space for alley, which width was taken from [4] and presented together with the trapezoid dimensions in Figure 28. During

every phase of the fuselage design, it was ensured that at every stage of loading there is a required clearance (specified by MIL-STD-1791A) between helicopter and the fuselage.

8.4 Pallet considerations

The pallet dimensions allowed them to fit within the perimeter of the Merlin helicopter. The pallets can be loaded and moved using rollers mounted on the fuselage floor. The pallets can be fastened using latches and/or specifically designed bolts. Due to proximity of the pallets in the layout (Figure 26), the fastening might not be simple and it has to be taken into consideration during detailed design of the fuselage floor and locking mechanisms.

8.5 Troops considerations

90 troops will be accommodated using palletized seating and 40 using side-wall seats (20 on each side). The seating pallets use 3 rows by 5 columns configuration. The pallet was designed using specifications in [4] for Business/DeLuxe seats. Such relatively large dimensions allow for comfortable flight as well as for extra space for stowing equipment. Although the fuselage layout requires design of a new pallet, there is a possibility of fitting already existing pallets, since most of them take less space than the customized one. Using the same seat dimensions as for the palletized seating, the seat pitch will allow space for alley and the seat width will allow for enough exit doors in the fuselage (see section 8.6).

8.6 Fuselage doors

The door and exit requirements for military aircraft are usually specified in the design requirements but in their absence, the FAR 25 specifications were used. For 110-139 passengers, the aircraft is required to have 2 exits of Type I and one exit of Type III on each side of the fuselage. Type III is specified with reference to "above wing" but mimicking the door layout of the Hercules C-130 [4], the reference to the wing was discarded from the design considerations. This resulted in the exit layout presented in Figure 31. The forward exit doors are located on the part of the fuselage that is referred to as the nose of the fuselage. This allows unobstructed evacuation for pilots even with Merlin helicopter fitted inside the fuselage. The dimensions of the exits used are presented in Table 26.

Table 26: Exit dimensions used. The type in the brackets corresponds to the FAR 25 exit type that dictates the minimum exit dimensions (see Reference [4]).

Exit Type	Width [in]	Height [in]	Corner radius [in]
A (Type I)	24	48	8.0
B (Type III)	20	36	6.7

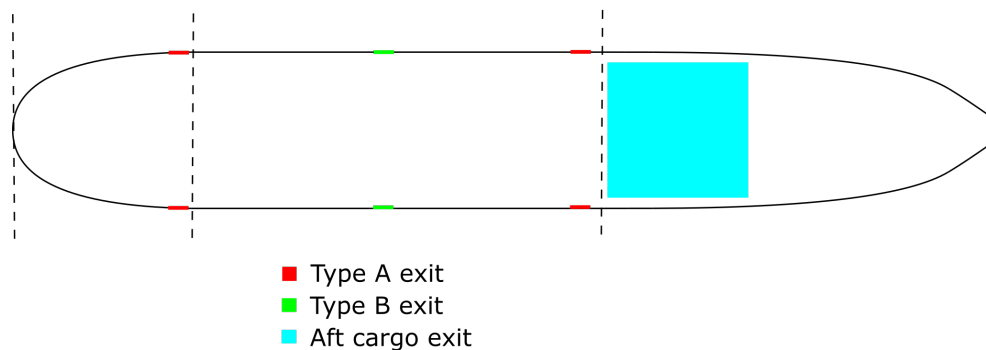


Figure 31: Fuselage exit door layout

8.7 Fuselage nose cone

The fuselage nose cone has to provide enough space for cockpit, nose landing gear, avionics and a radome. It also has to have appropriate shape so as to minimize drag. The side view of the fuselage nose is presented in Figure 32. It additionally shows the layout of the contents of the nose cone. It can be seen in the Figure

that part of the nose is marked as 'fuselage extension'. The nose is quite long and therefore there is some free space which cannot be used to carry cargo, but is instead used to hold the handling gear and give space for exit doors (see Section 8.6). The lavatory and the loadmaster station is also located in the cockpit. The essential windshield dimensions can be found in Figure 33.

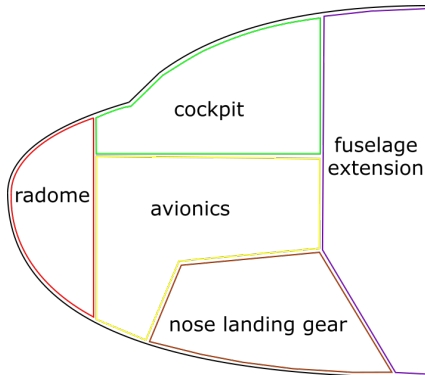


Figure 32: Side view of the fuselage nose

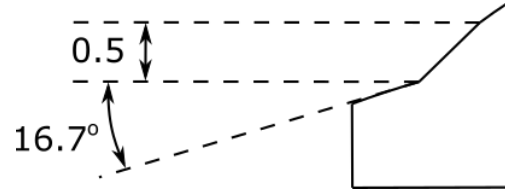


Figure 33: Cockpit windshield dimensions

8.8 Fuselage tail

The fuselage tail has to provide enough clearance for the loading as well as enough space for the APU with its fuel tank and structural depth [4] to support the empennage. The side view of the tail is presented in Figure 22. The main concern was the loading of the Merlin helicopter. This dictated a very long tail as well as larger fuselage diameter (look Section 8.3). The long fuselage tail has adverse effect on weight and skin friction drag but enables to have smaller empennage and decreased drag due to the tail upsweep. At this stage it is hard to design the fuselage opening mechanism but it will most probably be similar to the opening mechanism of the Hercules C-130. One part will move downwards to create a ramp and the necessary rest will hide inside the upper part of the tail.

9 Aircraft system layout design

9.1 Flight Control system

The flight control system provides crucial control over the movement of the aircraft. The aircraft will employ electrical signalling ("Fly-by-wire", see Section 9.6) to send commands to actuate every movement on the aircraft. Consequently, all the actuators on the aircraft will be powered using a hydraulic system (see Section 9.3). The flight control system will have a high degree of redundancy obtained using subdivision of control surfaces into smaller parts as well as due to usage of three independent hydraulic systems, three independent electronics systems and three independent avionic systems. The subdivision of control surfaces will provide a possibility to employ fewer models of actuators which will reduce design and maintenance costs [12]. Figure 34 presents the layout of control surfaces and their actuators. Due to the usage of "Fly-by-wire" control, the aircraft will not have any trim systems.

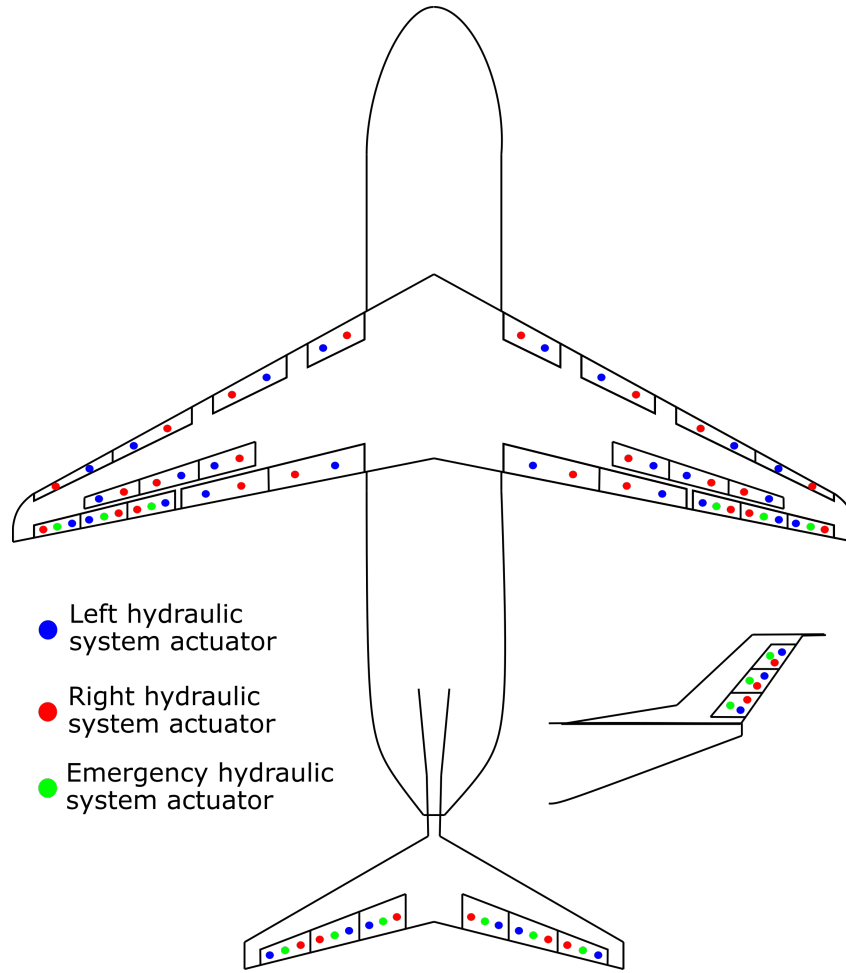


Figure 34: Actuators layout

9.2 Fuel system

The aircraft will use JP-8 fuel, as it is specified by the US military in MIL-DTL-83133. According to that specification at 15°C the JP-8 fuel density varies from 0.775 to 0.840 kg/L. Dividing the fuel weight (see Section 12.4) by the lower limit, the calculated fuel volume needed is 20.13 m³. The fuel will be accommodated using 4 main integral tanks in the wings located between the wing spars. The fuel tanks were modeled as truncated pyramids. The fuel tanks layout is presented in Figure 35 while the fuel flow diagram is shown in Figure 36. The tank volume available was calculated using CAD. The calculated volume is 24.48 m³ which leaves a good safety margin in case some space is taken by other systems components. Care was taken as to keep the bases of the truncated pyramid within the wing. The heights of the root base is 0.6 m and the outboard base height is 0.25 m, which is more than the heights of the spars at bases (root: 0.79 m, 0.88 m; outboard: 0.48 m, 0.48 m). There is a small cutout in the outboard fuel tank for engine dry bay. To maximize the available volume for fuel tanks in the wing, all subsystems components, where possible, are located in the fuselage ceiling unless stated otherwise. As is shown in Figure 36, the fuel system will enable to pump fuel between any two tanks, so as to enable more control over the position of the aircraft's CG. To prevent pressure build up in the tanks, each tank will have a venting mechanism. Additionally, to prevent the tanks overfilling as well as to collect any excess fuel vapor, surge tanks will be installed near the root - above the main tanks. An automated sumping system will be located at the bottom of the tanks to filter out any condensates. The fuel system will also include fuel jettison possibility.

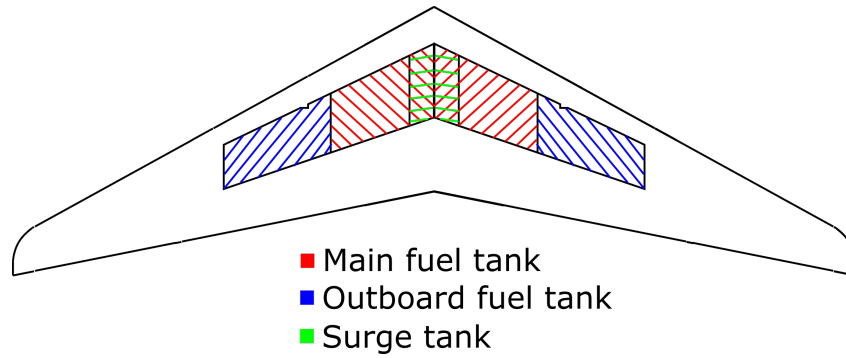


Figure 35: Fuel tanks layout

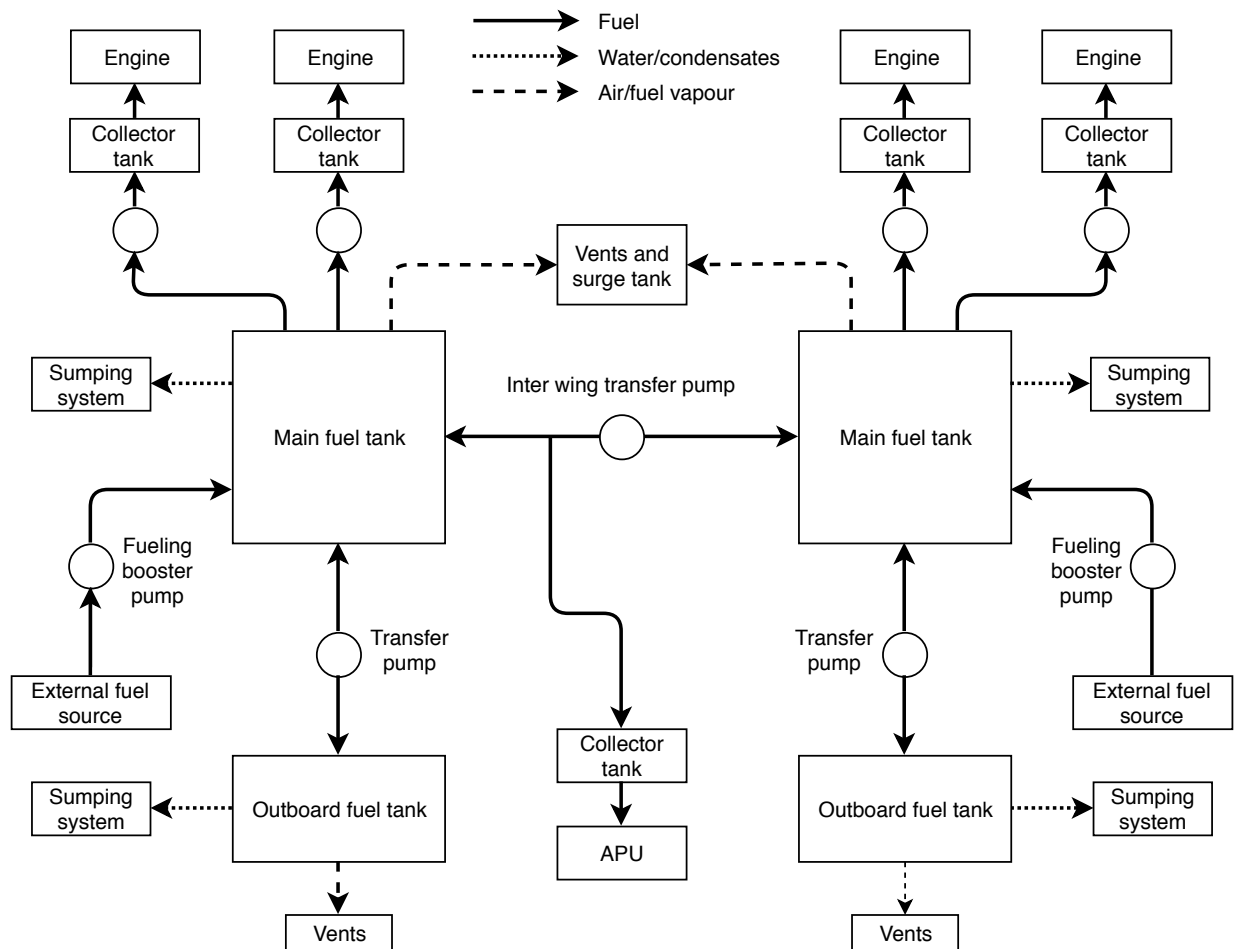


Figure 36: Fuel system schematic

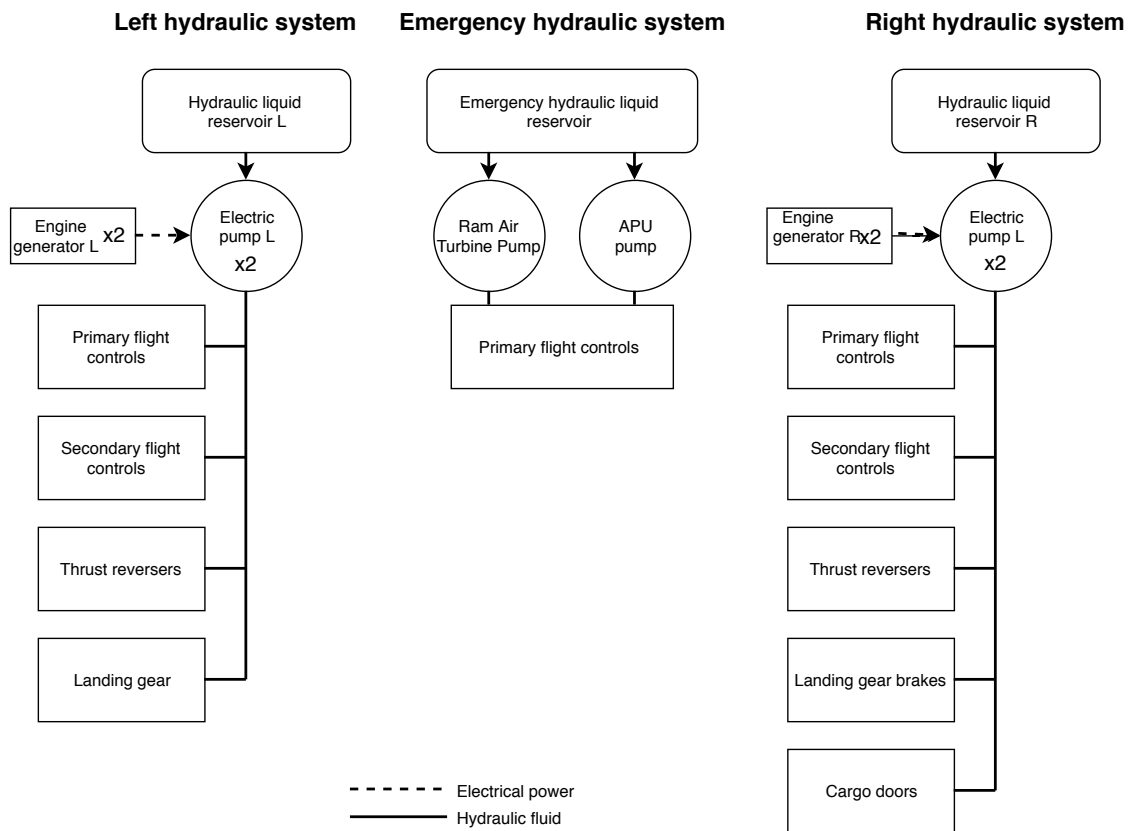


Figure 37: Hydraulic system schematic

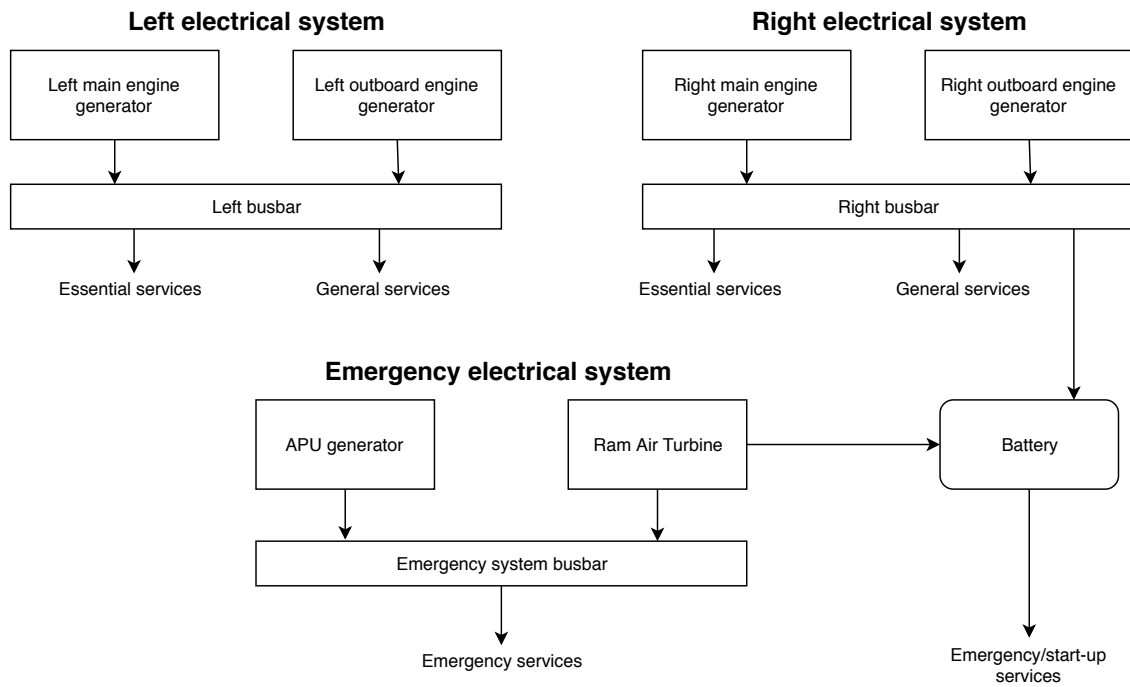


Figure 38: electrical system schematic

9.3 Hydraulic system

The hydraulic system provide a quick source of power to actuate any movement on the aircraft, be it the movement of control surfaces or undercarriage [12]. As mentioned earlier, the hydraulic system will consist of three independent systems. Figure 37 presents the hydraulic system schematic. The hydraulic oil lines will be located far from each other so as to decrease the probability of failure of both systems at the same time. Nevertheless, in the case of the emergency, the APU powered hydraulic system will be able to actuate enough control surfaces to maintain maneuverability of the aircraft. The system pumps will be driven electrically using six power sources. The hydraulic liquid containers as well as the pumps will be located in the ceiling of the fuselage.

9.4 Electrical system

The electrical system provides power to a number of systems on the aircraft [12]. In this aircraft it will be composed of three independent systems. The crude schematic of the electronic system is presented in Figure 38. It will be powered using 6 sources: 4 engine generators, APU generator and a Ram Air Turbine (RAT) which will be connected to a backup battery. To ensure the safety of the system, the electronic cables will be routed far away from each other in order to ensure that there will not be any electromagnetic interference between them. Both the RAT and the backup battery will be located under the cargo floor. Where applicable, all other electrical system components will be located in the ceiling of the fuselage.

9.5 Environmental control system

9.5.1 Pressurization system

The air needed for pressurization will be provided by the pneumatic system. The pressurization system will ensure appropriate pressure for comfort and safety for crew and the passengers on the aircraft. Computer controlled pressure relief valves will be located along the fuselage to provide both positive and negative pressure relief.

9.5.2 Pneumatic system

The pneumatic system provides air for the ECS systems as well as for the anti-icing. The air will be supplied from compressor stages of two engines closest to the fuselage as well as from the compressor stage of the APU.

9.5.3 Air-conditioning system

The air-conditioning system controls the temperature and humidity of the air inside the aircraft. The hot air supplied by the pneumatic system will be cooled down and distributed into the cabin for heating or cooling. As the aircraft has to be able to transport passengers, the fuselage cabin will be insulated. Additionally, the cockpit will be insulated from the cargo deck, to decrease the energy consumption while travelling without any passengers.

9.5.4 Oxygen system

For high altitude flight, FAR 25 specifies that the passengers must be provided with emergency oxygen in the event of unexpected cabin depressurization. The oxygen for the troops will be obtained using chemical generators and transferred to the troops using oxygen masks that will drop from the ceiling. The oxygen for the crew will be supplied using liquid oxygen tanks stored in the fuselage nose.

9.6 Avionics system

The avionics system will be contained within the fuselage nose cone as indicated in Figure 32. The avionics compartment will occupy extra space as to improve the layout of the avionics and simplify the maintenance of the system. To increase the degree of redundancy, command signals will be sent using three routes.

9.7 Other systems

9.7.1 Anti-icing system

The ice formation on the lifting surfaces will be prevented using a thermal anti-icing system. The hot air from the pneumatic system will pass through tubes located near the leading edges of wing and empennage. The hot air will also pass through the engine cowlings and pitot tubes. To de-ice the aircraft on the airstrip, external de-icing methods will have to be employed such as chemical de-icing.

9.7.2 Rain removal and defog system

The rain will be removed using wind-shield wipers and rain repellent. The windshield will be defogged using electrical heating.

10 Weight & balance predictions

The methods used for weight and balance predictions employ empirical equations and are described in detail in Reference [3]. The weight and balance calculation was done iteratively starting with the initial weight estimate from the Interim Poster. The other parameters were initially estimated using available methods but also refined with consecutive iterations. The final weight prediction and balance prediction results are presented in Table 28. All CG positions are measured from the nose of the aircraft.

10.1 CG envelope

Figure 39 presents CG envelopes for three loading cases for the mission profile.

Notes on weight & balance predictions

To decrease the weight of aircraft components, all possible fudge factors (presented in Table 27) were used. The CG position of the cargo was estimated to be 15 meters which corresponds to the middle of the fuselage cabin. The explanation for each CG position is tabulated in Table 29.

Table 27: Weight estimation "fudge factors" due to the application of advanced materials [3].

Component	Fudge factor
Wing	0.85
Tails	0.83
Fuselage/Nacelle	0.9
Undercarriage	0.95
Air induction system	0.85

Table 28: Component weight and x-CG positions

Component	Weight [kg]	x-CG position [m]
Wing	6260	19.1
Horizontal tailplane	663	42.0
Vertical tailplane	705	37.0
Fuselage	9240	15.4
Main landing gear	2340	17.2
Nose landing gear	116	4.0
Engines	3470	16.1
Nacelle	1460	16.1
Engine controls	122	16.1
Engine starter	86.8	16.1
Fuel system	202	17.7
Flight controls	851	23.7
Installed APU	308	37.4
Instruments	238	3.0
Hydraulic system	308	20.0
Electrical system	938	20.0
Avionics	903	3.0
Furnishings	2030	15.4
Air-conditioning	591	15.4
Anti-icing	150	22.9
Handling gear	519	15.0
Empty weight	6940	N/A
Fuel	N/A	12.9
MTOW	74800	N/A
TOW case: helicopter	50800	N/A
TOW case: pallets	74800	N/A
TOW case: troops	64300	N/A

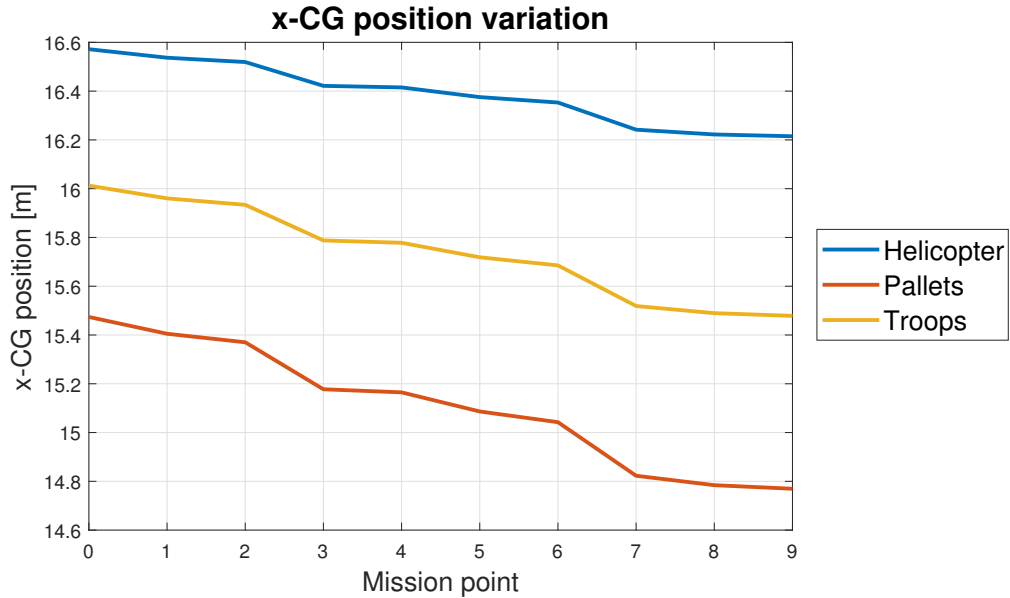


Figure 39: Variation of x-CG position during mission for three loading cases

Table 29: Reasoning behind estimating CG positions of aircraft components

Component	Explanation
Wing	Estimated numerically
Horizontal tail	Estimated using CAD model (40% of MAC [3])
Vertical tail	Estimated using CAD model (40% of MAC [3])
Fuselage	40% of fuselage length [3]
Main landing gear	Estimated using [13]
Nose landing gear	Estimated using cockpit layout in Figure 32
Engines	Estimated using CAD model (50% of engine length)
Nacelle	Same as the engine
Engine controls	Same as the engine
Engine starter	Same as the engine
Fuel system	Estimated using CAD model of fuel tanks
Flight controls	Weighted average of the wing and tail CG positions
Installed APU	Fuselage length minus 50% of APU length
Instruments	Inside the cockpit
Hydraulic system	Weighted average estimated using hydraulic system layout
Electrical system	Weighted average estimated using electrical system layout
Avionics	Inside the cockpit (contribution of signalling cables was neglected)
Furnishings	40% of fuselage length [3]
Air-conditioning	40% of fuselage length [3]
Handling gear	40% of fuselage length [3]
Cargo	50% of fuselage cabin

11 Aerodynamic analysis - Drag Estimation

Drag on the aircraft was calculated for cruise, take-off and landing, taking care of including effects of viscosity, vortex sheets and shock waves. Drag was therefore divided in three components: parasite drag, lift-induced drag, and finally wave drag which may occur as we approach the transonic region. Unless clearly stated, the methods and equations used for drag estimation can be found in Reference [3], and therefore will not be extensively re-derived here.

11.1 Parasite (Zero-Lift) Drag Prediction

Parasitic drag was estimated using the component buildup method, introduced in Equation (11).

$$C_{D0_{subsonic}} = \frac{\sum C_{fc} FF_c Q_c S_{wet_c}}{S_{ref_c}} + C_{D_{misc}} + C_{D_{L\&P}} \quad (11)$$

11.1.1 Main Components

To account for the main components of the aircraft, flat-plate skin friction coefficients C_{fc} and form factors FF_c were calculated for each component, and used with their corresponding interference factors Q_c and wetted area S_{wet_c} to obtain the first term on the RHS of Equation (11). C_{fc} were calculated for both laminar and turbulent regimes, and final C_{fc} taken as a 99% contribution from turbulent regime for only 1% from laminar. The values used are presented in Tables 30, 31 and 32.

Table 30: Values of coefficients used in Equation (11) for parasitic drag of main components.

	Wing	Fuselage	Tail	Pod	Nacelle
FF_c	1.5618	1.1912	1.7485	26.3158	1.1902
Q_c	1	1	1.05	1.5	1.5
S_{wet_c}	4520.8	8072.9	3243.7	45.088	38.556

Table 31: Values of friction and drag coefficients for subsonic cruise at Mach number $M = 0.79$. S_{ref} used to obtain C_{D0_c} is $2260.4ft^2$. To account for possible roughness of surfaces, C_{f_c} were computed using the lowest of actual and cut-off Reynolds numbers for each components, as explained in Reference [3].

	Wing	Fuselage	Tail	Pod	Nacelle
C_{f_c}	0.0026	0.0019	0.0027	0.0030	0.0028
C_{D0_c}	0.008	0.0082	0.0071	0.0024	0.0001
Total C_{D0}	0.0306				

Table 32: Values of friction and drag coefficients for subsonic take-off and landing. S_{ref} used to obtain C_{D0_c} is $2260.4ft^2$. Values for take-off and landing are rather close as the Mach numbers at Mach number $M = 0.17$ at these points of the mission are very close.

	Wing	Fuselage	Tail	Pod	Nacelle
C_{f_c}	0.0025	0.0019	0.0026	0.0029	0.0027
C_{D0_c}	0.0077	0.0080	0.0069	0.0023	0.0001
Total C_{D0}	0.0296				

Note that to calculate C_{D0} , pods and nacelle contributions had to be multiplied by the number of elements. Also, the high contribution from the tail can be explained by the selection of a T-Tail, and therefore the presence of both horizontal and vertical surfaces.

11.1.2 Miscellaneous Drags

Miscellaneous parts of the aircraft are accounted separately, mainly using empirical equations. The values calculated are presented in Table 33. Effect of the fuselage upsweep angle were accounted using a different method than the one proposed in reference [3], however computed and used for comparison. Where Reference [3] mainly takes account of the maximum cross-sectional area of the fuselage and its rear sweep angle to build the empirical equation used, the method in Reference [14] uses the length and diameter at 75% of the upsweep length section, and results from more recent wind-tunnel measurements. It was therefore chosen for the sake of accuracy. However, the 0.11% variance between both results was found to be really low, as the method in [3] gave a $C_{D0_{misc,upsweep}}$ of 0.0093 while method in [14] gave 0.0083.

Table 33: Values of miscellaneous drag coefficients for different components in the subsonic regime.

	Upsweep (24°)	Undercarriage (6 wheels)	Flaps		Speedbrakes	Windshield
$C_{D0_{misc}}$	0.0078	0.0030	take-off: 25° 0.0345	landing: 35° 0.0483	0.0048	0.0040

By summing the appropriate components for each part of the flight, $C_{D0_{misc,total}}$ was computed for cruise, take-off and landing.

Table 34: Total miscellaneous drag coefficients for three phases of the flight: cruise, take-off and landing. Note that take-off and even more particularly landing have high values due to the high deflection of the flaps.

	Cruise	Take-off	Landing
Total $C_{D0_{misc}}$	0.0119	0.0494	0.0679

11.1.3 Leakage and Protuberance Drag

Finally, 5% of the calculated C_{D0} was added in order to account for leakage and protuberance, most likely to occur notably due to the mechanism of rear opening to unload the aircraft. This drag component is due to the tendency of the aircraft to flow leakage into gaps in high-pressure areas, leading to an overall loss in momentum. However, special care taken to keep smooth surfaces, and the decision of a rear-opening system kept in the shadow of other surfaces allows to reduce impact of those momentum losses and separation, and therefore makes the estimation of $C_{D_{L\&P}}$ as only 5% of C_{D0} safe.

11.2 Induced (Lift Dependant) Drag

The induced drag was then calculated to account for the components of lift opposing the thrust. The classical method based upon the Oswald span efficiency factor e was used and compared to a leading-edge-suction method, also accounting for ground effects during landing and take-off. Results are summarised in Table 35, and contain contributions from both wing and tail, with Oswald efficiencies found to be respectively equal to $e_w = 0.8082$ and $e_t = 0.8421$ for the first method, and a tail efficiency of $\eta = 0.9$.

Table 35: Values of induced drag coefficients from Oswald efficiency based and suction methods. Values for cruise are different as the drag-due-to-lift factors K are obtained by different ways. Also, take-off and landing values are higher for the suction method, which also includes ground effects, generating more lift.

	Cruise	Take-off	Landing
$C_{D_{ie}}$	0.0075	0.3328	0.3927
$C_{D_{is}}$	0.0064	0.4073	0.4809

Note that the values found with the first method can be slightly overestimated as the Oswald efficiencies seem rather low.

11.3 Wave drag

As the design Mach number for cruise was imposed to be 0.79, effects of compressibility in the transonic regime had to be addressed. Drag divergence Mach numbers were empirically estimated for both wings and fuselage, and found to be equal to $M_{DD_w} = 0.796$ and $M_{DD_f} = 0.830$ from graphical readings of Figures 12.17 and 12.28, and approximation from Equation (12.47) in Reference [3]. The thickness to chord ratio of the wing $\frac{t}{c} = 0.1$ was multiplied by 0.6 due to the use of a supercritical airfoil, and the length L_n at which the cross-sectional area of the fuselage becomes constant is exactly equal to 7 meters.

A second method [15], used only for the sake of comparison, gave $M_{DD_w} = 0.813$ from Equation (12) below, using the factor established through CFD analysis $K = 0.95$ for supercritical airfoils.

$$M_{DD} = -\frac{C_{L_{design}}}{10} + C_{D_{misc}} - \frac{t}{c} + K \quad (12)$$

The wing would therefore most probably experience drag before the fuselage in our case. Calculation of wave drag were then performed using Korn equation [15], shown below:

$$C_{D_{wave}} = 20 \cdot (M - M_{crit})^4 \cdot \frac{S_{strip}}{S_{ref}} \quad (13)$$

where

$$M_{crit} = M_{DD} - \left(\frac{0.1}{80}\right)^{\frac{1}{3}} \quad (14)$$

Taking $\frac{S_{strip}}{S_{ref}} = \frac{1}{3}$ as a first approximation, we find for $M = 0.79$:

$$C_{wave,w} = 0.00071 \quad ; \quad C_{wave,f} = 0.00014$$

while for $M = 0.82$:

$$C_{wave,w} = 0.0020 \quad ; \quad C_{wave,f} = 0.00061$$

The choice of a supercritical airfoil shall delay the onset of wave drag enough to lead a rather small wave drag contribution for an aircraft designed to operate in the lower part of the transonic range such as ours. However, as these results seemed rather low, a rough but safe estimation of $C_{D_{wave}} = 0.002$ was kept and added for the rest of the analysis.

11.4 Total Drag Coefficient

Once the different components of drag were calculated, a simple summation allowed to obtain the total drag coefficients for the three sections of the flight. These are shown in Table 36 below. The mean variance between $C_{D_{total}}$ resulting from both methods for induced drag is of 5.3%.

Table 36: Values of drag coefficients, using both Oswald efficiency based and suction method for C_{D_i} . Values of $C_{D_{total}}$ for take-off and landing are notably high, which could be explained by the flaps deflection impacting C_{D_0} and the lift generated impacting C_{D_i} .

	Cruise	Take-off	Landing
$C_{D_{0total}}$	0.0446	0.0830	0.1024
$C_{D_{ie}}$	0.0075	0.3328	0.3927
$C_{D_{is}}$	0.0064	0.4073	0.4809
C_{D_w}	0.002	N/A	N/A
$C_{D_{total,e}}$	0.0521	0.4158	0.4951
$C_{D_{total,s}}$	0.0510	0.4903	0.5833

12 Performance Estimation

Field performance relies on three main components: take-off distance, balanced field length, and landing distance. These values have to be found in order to ensure the ability of the aircraft to perform the mission within the constraints set by the run-way geometry and FAR-25 considerations. Unless clearly stated, the method follows References [3] and [16].

12.1 Take-off distance

The aircraft should be able to take-off within the first 1.5km runway, but also within the more constraining 1km semi-prepared runway between the two cruises. The take-off segment can be broken down into four segments: ground roll distance S_G , rotation distance S_R , transition distance S_{TR} , and climb distance S_{CL} . Taking a 1.15 safety factor, the final take-off distance is simply given by Equation (15):

$$S_{TO} = 1.15 \cdot (S_G + S_R + S_{TR} + S_{CL}) \quad (15)$$

The conditions must be taken at corresponding points of the mission: maximum thrust at sea level, aircraft take-off weights corresponding to $TOW_1 = MTOW = 733788N$ for first take-off, and using the weight fractions to obtain second take-off weight $TOW_2 = 650060N$, deployed flaps, lift coefficient at take-off. Note that in the following section, subscripts 1 and 2 refers to values at first and second runways respectively.

12.1.1 Ground Roll S_G

The rolling resistances were taken to be 0.05 for the first take-off and 0.07 for the second take-off, for hard turf/concrete and soft turf respectively, as Reference [3] advises. Initial velocity V_1 was set to 0, and $V_2 = 1.1 \cdot V_{stall}$ where $V_{stall,1} = 48.11m \cdot s^{-1}$ for the first take-off, giving $V_{2,1} = V_{TO,1} = 52.92m \cdot s^{-1}$. Similarly, $V_{stall,2} = 45.28m \cdot s^{-1}$ for the second take-off, giving $V_{2,2} = V_{TO,2} = 49.81m \cdot s^{-1}$. These were evaluated at $C_{L,max,TO}$ and take-off wing loadings. We find:

$$S_{G_1} = 619.56m \quad ; \quad S_{G_2} = 469.04m$$

Where the difference can be explained by the difference in weights due to the amount of fuel lost during the first cruise, which has more impact here than the difference in rolling resistance of the two runways. The distances however seem a bit low, which could be explained by the low empty weight of the aircraft.

12.1.2 Rotation distance S_R

Assuming a negligible acceleration over that short time interval, and a rotational time of three seconds - which guarantee safety factor as military pilots usually have lower reaction times - for large aircrafts, we find, by multiplying the latter by V_{TO} :

$$S_{R_1} = 162.98m \quad ; \quad S_{R_2} = 153.40m$$

12.1.3 Transition distance S_{TR}

The aircraft needs to accelerate from take-off speed V_{TO} to climb speed $V_{climb} = 1.2 \cdot V_{stall}$. Taking the average velocity during transition as $V_{TR} = 1.15 \cdot V_{stall}m \cdot s^{-1}$, we find $V_{TR,1} = 55.32m \cdot s^{-1}$ and $V_{TR,2} = 52.08m \cdot s^{-1}$. The maximum climb angle γ_{climb} can be found from geometry, and used to find the transition segment length, giving:

$$\gamma_{climb,1} = 17.24^\circ \quad ; \quad \gamma_{climb,2} = 20.07^\circ$$

$$S_{TR_1} = 162.98m \quad ; \quad S_{TR_2} = 153.40m$$

12.1.4 Climb to obstacle height S_{CL}

The climb angle γ_{climb} can also be used to find out if the obstacle height is cleared before the end of the transition segment, by finding the altitude h_{TR} gain during transition. We find:

$$h_{TR,1} = 73.85m \quad ; \quad h_{TR,2} = 99.80m$$

The 50ft obstacle clearance required by FAR25 is therefore met, as the aircraft is able to clear an obstacle as high as 97.45ft. Therefore, the climb to obstacle height S_{CL} is set to zero. Note however that the values of climb angles should be set to lower values in order to avoid stall. Imposing $\gamma_{climb} = 13^\circ$, which is way below our stall climb angle, $h_{TR} = 42.14m$, and the obstacle clearance is still verified.

12.1.5 Total take-off distances

Table 37: Values of take-off distances and their components for both runways. Distances are in meters. A safety factor of 1.5 was applied. Both S_{TO} are smaller than their respective runways, of 1.5km and 1km. Therefore, both take-off can be achieved.

	Rolling resistance μ	S_G	S_R	S_{TR}	S_{CL}	Total S_{TO}
Take-off from prepared runway	Dry concrete / hard turf 0.05	619.57	162.98	223.34	0	1156.8
Take-off from semi-prepared runway	Soft turf 0.07	469.04	153.40	210.15	0	957.47

12.2 Balanced Field Length

Once we made sure take-off can be achieved within the imposed distances, the next step was to check if the aircraft was able to take-off and clear the 50ft high obstacle after failure of one engine at V_x , where V_x is the speed at which the aircraft can either brake to a halt or continue the take-off in the same total distance. Before that speed, the pilot can easily brake to an halt, and after that speed, he musts continue the take-off. The corresponding distance is the balanced field length BFL. Using Equation (17.110) in Reference [3], taking particular attention to the units of each term, and using C_L value with the flaps deployed in the equation for U, we find $BFL = 1298.4$ m, which is a sensible value for a runway of 1.5km. The climb angle with one engine off $\gamma_{climb,OEI}$ was found to be 0.2661 (15.25°), for $\gamma_{min} = 0.03$ for a four-engines aircraft.

12.3 Landing Distance

Finally, we need to make sure the aircraft is able to land within the first 1.5km runway, but also within the more constraining 1km semi-prepared runway between the two cruises. The landing segment can be broken down into four segments: approach S_A , flare S_F , free roll S_{FR} , and braking distance S_B . The final landing distance is simply given by Equation (16), multiplied by 1.666 for the landing on the prepared runway, and using thrust reversers for the semi-prepared runway :

$$S_L = S_A + S_F + S_{FR} + S_B \quad (16)$$

The conditions must be taken at corresponding points of the mission: using the weight fractions to obtain landing weights, deployed flaps, lift coefficient at landing. Note that in the following section, subscripts 1 and 2 refers to values at first prepared and second semi-prepared runways respectively.

12.3.1 Approach

The same way the take-off ends, landing starts with obstacle clearance over 50ft. Taking the approach speed V_a as 1.2 times the stall speed, we find $V_{a,1} = 59.27m.s^{-1}$ and $V_{a,2} = 55.78m.s^{-1}$. The steepest approach with drag and full flaps deflected can therefore be found, and used to compute the approach distance:

$$S_{A_1} = 254.99m \quad ; \quad S_{A_2} = 250.11m$$

12.3.2 Flare

During the flare, the aircraft decelerates from approach speed V_a to touch down speed $V_{TD} = 1.1 \cdot V_{stall}$. We can find the flare horizontal distance by taking the average flare velocity as $V_f = 1.15 \cdot V_{stall}$ to find the flare radii $R_{F,1} = 1456.5m$ and $R_{F,2} = 1644.1m$ by geometry, and plug in Equation (17.106) of Reference [3], giving:

$$S_{F_1} = 75.71m \quad ; \quad S_{F_2} = 85.46m$$

12.3.3 Rolling

After the aircraft touches the ground, it will roll for a small amount of time before brakes are applied. This delay t_{FR} mainly depends on the pilot, and is taken to be of approximately 2 seconds, which gives a safety margin as military pilots usually have shorter response reactions. This delay can be multiplied by the velocity of the aircraft during this free rolling, taken as $V_{TD} = V_S$, to get the free roll distance:

$$S_{FR_1} = 102.27m \quad ; \quad S_{FR_2} = 108.65m$$

12.3.4 Braking

After this short delay, when brakes are on, the aircraft will decelerate from V_{TD} to complete standstill. The rolling resistances μ for landing on the prepared and semi-prepared runway are respectively taken to be 0.2 and 0.4. The same equation as the one used to obtain the take-off ground roll distance in section 12.1.1 was used to find:

$$S_{B_1} = 355.09m \quad ; \quad S_{B_2} = 434.29m$$

12.3.5 Total landing distances

Table 38: Values of landing distances and their component for both runways. Distances are in meters. Both S_L are smaller than their respective runways, of 1.5km and 1km. Therefore, both landings can be achieved.

	Rolling resistance with brakes on μ	S_A	S_F	S_{FR}	S_B	Total S_L
Landing on prepared runway	Dry concrete / hard turf 0.2	254.00	75.71	102.27	355.09	1312.90
Landing on semi-prepared runway	Soft turf 0.4	250.11	85.46	108.65	434.29	878.51

12.4 Mission performance

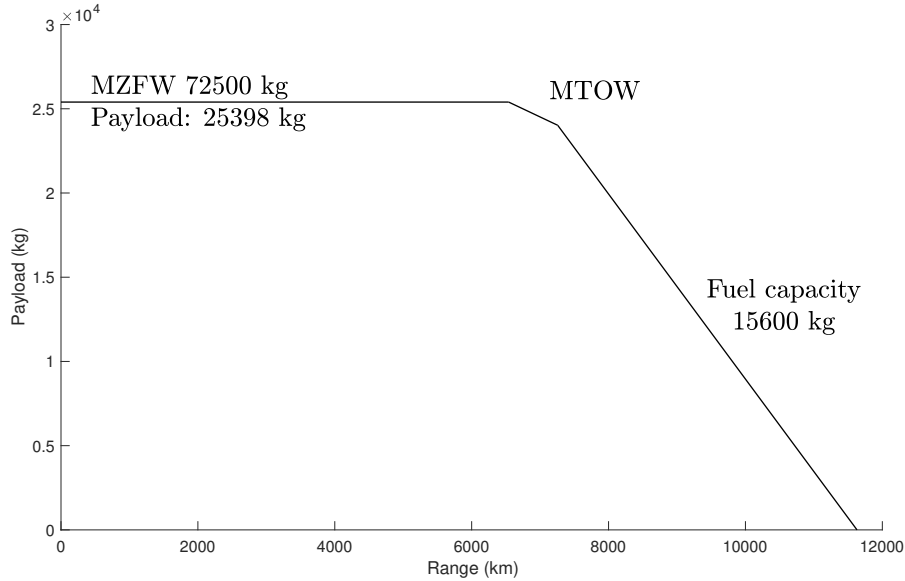


Figure 40: Cruise range performance

As seen in Figures 40, the maximum achievable range carrying the highest payload is 6540.4 km, which allows the aircraft to achieve the mission imposed, including a loiter. With the maximum amount of fuel that can be stocked in the tanks, and an additional payload to attain the maximum take-off weight, the range becomes 7257.1 km: i.e an increase of only 10.96%. This can be explained by the small volume of tanks chosen, which means the maximum fuel capacity is rather close to the fuel needed to be carried to complete the mission with our highest payload. Finally, the range with no payload and full fuel tanks is of 11630 km. Noting for comparison that the range of the McDonnell Douglas C-17 Globemaster III is of 10390 km, 11705 km for the Lockheed C-5 Galaxy,

12.5 Point performance

By definition, absolute ceiling can be found when the vertical velocity V_v is equal to zero, and the service ceiling when it is equal to approximately $500 \text{ ft} \cdot \text{min}^{-1}$. The absolute ceiling was found to be 51300 ft, and the maximum service ceiling 47900 ft. This can be observed on the graph in Figures 41, in section 12.6.

12.6 Flight envelope

The flight envelope could be found by calculating the excess power P_S available, and therefore the vertical velocity V_v the aircraft is able to reach. This was made by varying both altitude and Mach number, and

therefore thrust, following Equation (17) from sea level to the end of the troposphere (i.e 11km) and Equation (18) in the stratosphere. Subscripts 0 refers to sea level and h to position altitude.

$$T = T_{max,0} \cdot \left(\frac{\rho_h}{\rho_0} \right)^{0.7} \quad (17)$$

$$T = T_{max,0} \cdot \frac{\rho_h}{\rho_0} \left(\frac{\rho_{11km}}{\rho_0} \right)^{-0.3} = 1.439 \cdot \frac{\rho_h}{\rho_0} \quad (18)$$

Taking a drag divergence Mach number $M_{DD} = 0.8$ by averaging the values estimated in section 11.3, wave drag was added to overall drag and can be seen to affect the right part of the plot, by creating irregularities in excess power and deficit in available V_v . Absolute ceiling and service ceiling can be read from this graph, as well as safe flying regions, avoiding the stall line vicinity.

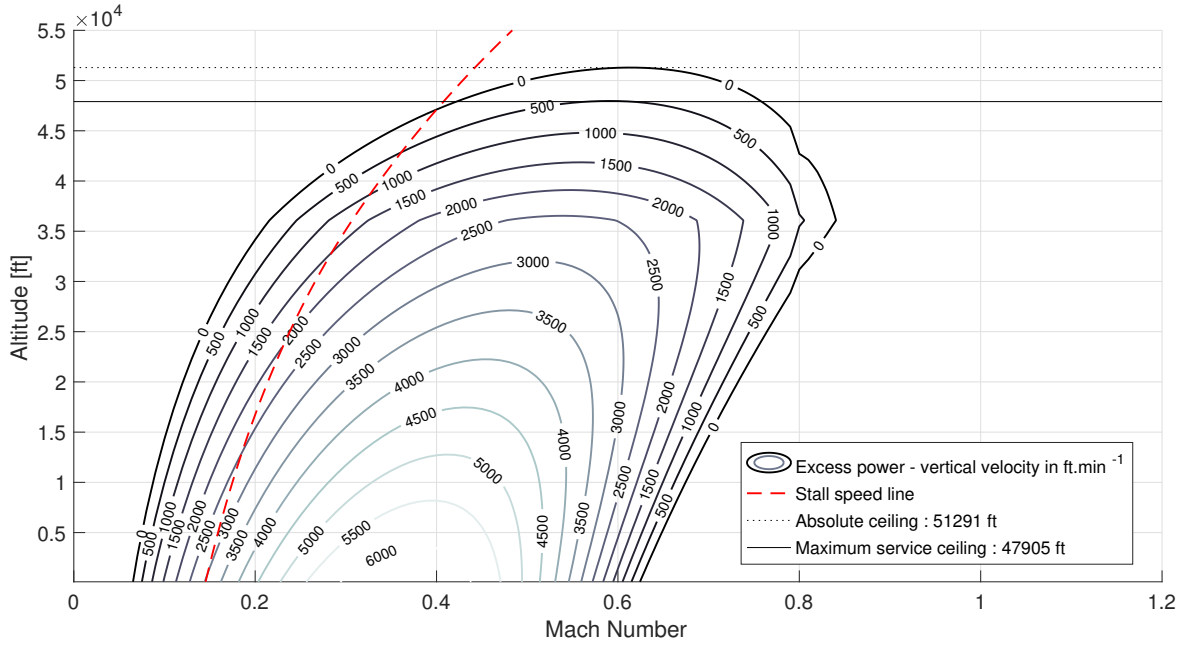
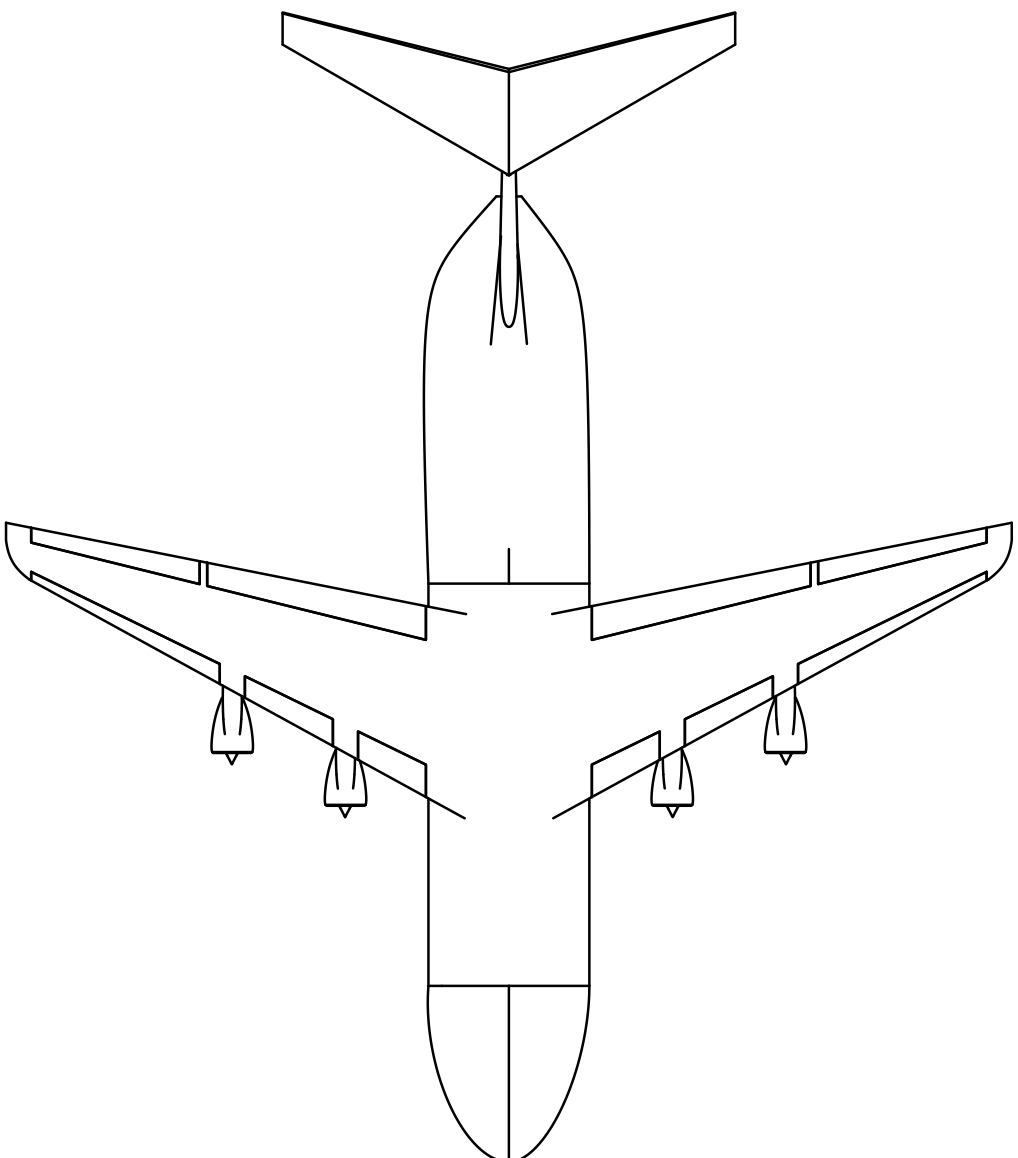
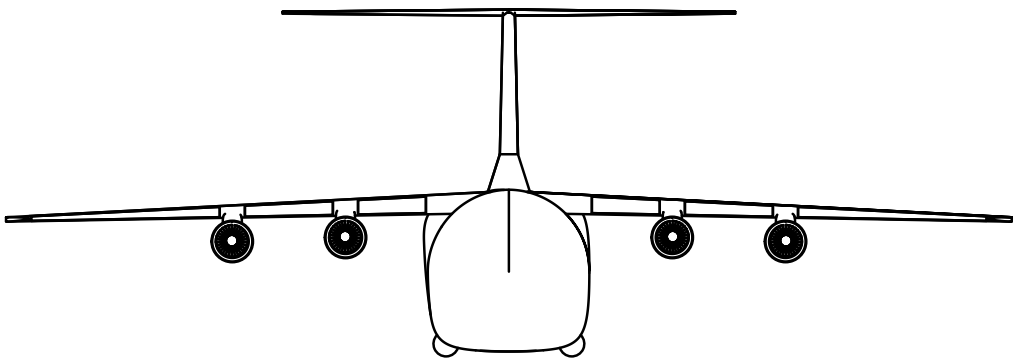


Figure 41: Excess Power P_S plot, in $\text{ft} \cdot \text{min}^{-1}$

References

- [1] Polhamus TA E C ; Toll. (NASA-TM-83121) Research related to variable sweep aircraft development. 1981;.
- [2] Loftin J Lawrence K. (NASA-SP-468) Quest for Performance: the Evolution of Modern Aircraft. 1985;.
- [3] Raymer a Daniel P. Aircraft design : a conceptual approach. Fifth edition. ed. AIAA education series. Reston, Virginia: American Institute of Aeronautics and Astronautics; 2012.
- [4] Roskam J. Airplane design. Part 3, Layout design of cockpit, fuselage, wing and empennage : cutaways and inboard profiles. Ottawa: Roskam Aviation and Engineering Corporation; 1986.
- [5] Harris CD. (NASA-TP-2969) NASA supercritical airfoils: A matrix of family-related airfoils. 1990;.
- [6] Anderson JD. Introduction to flight. 7th ed. New York : London: McGraw-Hill Higher Education ; McGraw-Hill; 2011.
- [7] Roskam J. Airplane design. Part 6, Preliminary calculation of aerodynamic, thrust and power characteristics. Ottawa: Roskam Aviation and Engineering Corporation; 1987.
- [8] Sadraey MH. Aircraft design : a systems engineering approach. Hoboken, New Jersey: Wiley; 2012.
- [9] Roskam J. Airplane Design. Pt. 2. Preliminary Configuration Design and Integration of the Propulsion System. Roskam Aviation and Engineering; 1985.
- [10] Levis DE. Aerospace Vehicle Design Flying Surface Design, Department of Aeronautics, Imperial College London, SW7 2AZ London. 2018;.
- [11] Levis DE. Aerospace Vehicle Design Stability, Control and Handling Qualities, Department of Aeronautics, Imperial College London, SW7 2AZ London. 2018;.
- [12] Roskam J. Airplane design. Part 4, Layout design of landing gear and systems. Ottawa: Roskam Aviation and Engineering Corporation; 1986.
- [13] Mason WH, Chai ST. Landing Gear Integration in Aircraft Conceptual Design - NASA-CR-205551; 1997. Available from: <http://hdl.handle.net/2060/19970031272>.
- [14] Stanford. Technical Status Review on Drag Prediction and Analysis from Computational Fluid Dynamics. AGARD AR 256. 1989;.
- [15] Boppe TA C W ; Toll. CFD Drag Prediction for Aerodynamic Design;.
- [16] Levis DE. Aerospace Vehicle Design Performance Estimation, Department of Aeronautics, Imperial College London, SW7 2AZ London. 2018;.

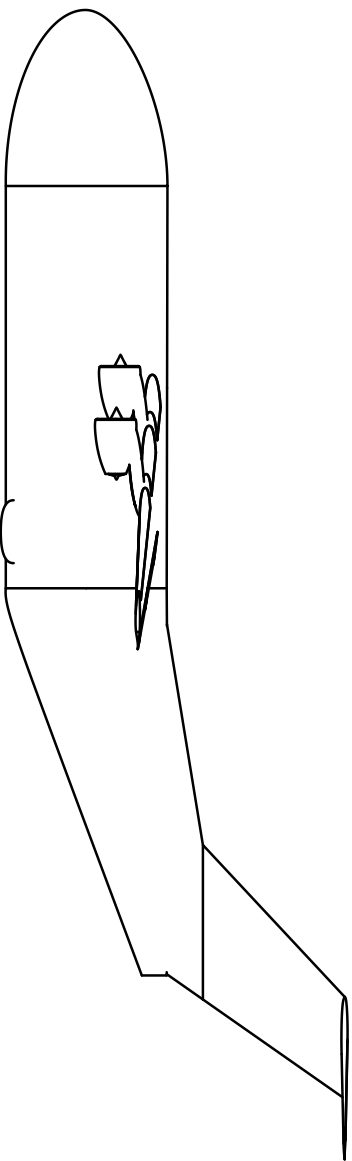


Aerospace Vehicle Design Project

Group 14

scale: 0.005

date: 05.12.2018

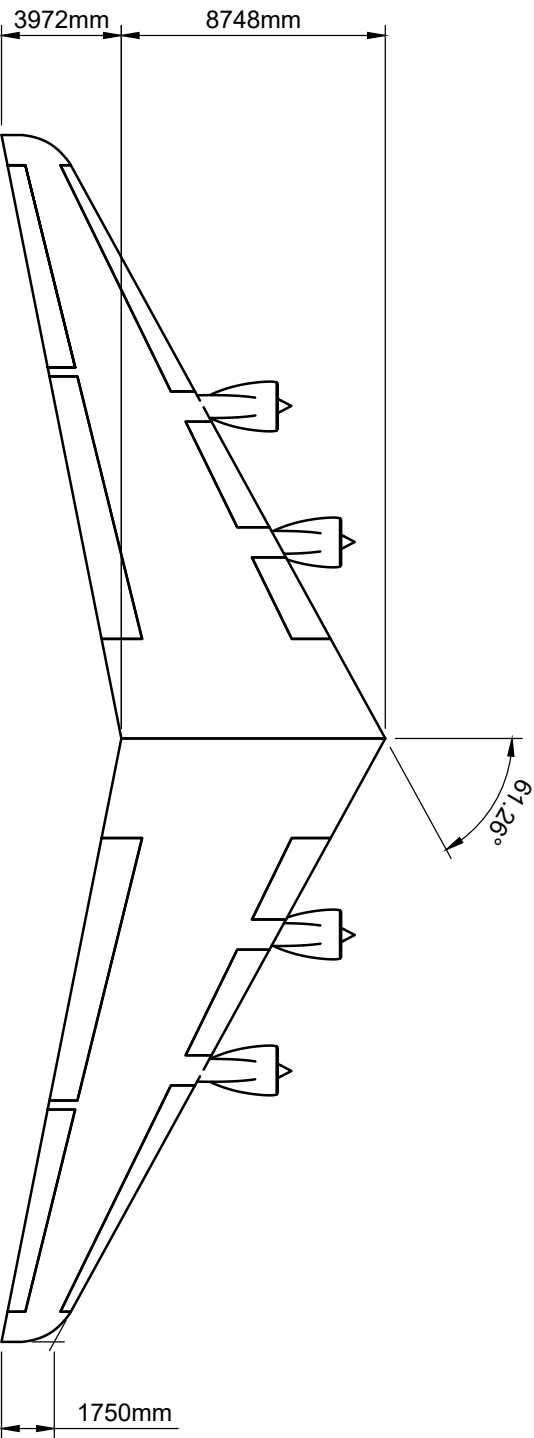


Aerospace Vehicle Design Project

Group 14

scale: 0.005

date: 05.12.2018



Planform area=209.95 m²
Dihedral = -2°
Aspect Ratio = 7.62

Aerospace Vehicle Design Project			
Group 14		scale:	0.005
		date:	05.12.2018